

# Earth and Space Science



## RESEARCH ARTICLE

10.1029/2022EA002287

### Key Points:

- This study reveals that the below-cloud aerosols may share similar properties with those without overlying clouds
- The wide coverage of the below-cloud aerosols indicates a likely significant impact of cirrus on aerosol direct radiative effect
- Regional and seasonal variations of the cloud-free and cloudy aerosols strongly depend on the local climate and long-range transport

### Correspondence to:

Y. Hong,  
[yulanh@illinois.edu](mailto:yulanh@illinois.edu)

### Citation:

Hong, Y., & Di Girolamo, L. (2022). An overview of aerosol properties in clear and cloudy sky based on CALIPSO observations. *Earth and Space Science*, 9, e2022EA002287. <https://doi.org/10.1029/2022EA002287>

Received 15 FEB 2022

Accepted 22 MAR 2022

### Author Contributions:

**Conceptualization:** Yulan Hong, Larry Di Girolamo  
**Formal analysis:** Yulan Hong  
**Funding acquisition:** Larry Di Girolamo  
**Investigation:** Yulan Hong  
**Methodology:** Yulan Hong, Larry Di Girolamo  
**Supervision:** Larry Di Girolamo  
**Validation:** Yulan Hong  
**Visualization:** Yulan Hong  
**Writing – original draft:** Yulan Hong  
**Writing – review & editing:** Yulan Hong, Larry Di Girolamo

© 2022 The Authors. *Earth and Space Science* published by Wiley Periodicals LLC on behalf of American Geophysical Union.

This is an open access article under the terms of the Creative Commons Attribution-NonCommercial-NoDerivs License, which permits use and distribution in any medium, provided the original work is properly cited, the use is non-commercial and no modifications or adaptations are made.

## An Overview of Aerosol Properties in Clear and Cloudy Sky Based on CALIPSO Observations

Yulan Hong<sup>1</sup>  and Larry Di Girolamo<sup>1</sup> 

<sup>1</sup>Department of Atmospheric Sciences, University of Illinois Urbana-Champaign, Urbana, IL, USA

**Abstract** A full understanding of the climatological properties of aerosols is an important step towards characterizing their effects on climate. Utilizing the observations from Cloud-Aerosol Lidar and Infrared Pathfinder Satellite Observations, we study cloud-free and cloudy aerosol properties with attention on aerosol and cloud layer relative vertical positions. On a global scale, the cloud-free aerosols account for about 56% of all detected aerosols with a mean optical depth ( $\bar{\tau}_a$ ) and mean uncertainty of  $0.135 \pm 0.047$ . The cloudy aerosols, accounting for 44%, have a larger  $\bar{\tau}_a$  and larger mean uncertainty of  $0.143 \pm 0.074$  compared to the cloud-free aerosols. The above-cloud aerosols (~4%), primarily composed of elevated smoke, dust/volcanic ash and polluted dust, have a much smaller  $\bar{\tau}_a$  of  $(0.056 \pm 0.038)$ . The below-cloud aerosols (~21%) have  $\bar{\tau}_a \sim 0.165 \pm 0.087$ . The below-cloud and cloud-free aerosols show close  $\tau_a$  probability density distributions and similar aerosol types, indicating that cloud-free aerosol climatologies from passive sensors are likely representative of all-sky conditions. In addition, about 27% of the detected aerosol profiles are found to have cloud layers vertically connected to the detected aerosol layers. The lidar backscatter profiles of these aerosols have larger median values than the cloud-free, above-cloud and below-cloud aerosols. The seasonal variations of the cloud-free and the cloudy aerosols significantly vary with regions. Our results imply that quantifying the impact of clouds, particularly cirrus due to the wide coverage of cirrus-aerosol overlap, on aerosol direct radiative effect is crucial to assess aerosols' roles in the Earth-climate system.

## 1. Introduction

Aerosols influence Earth's weather and climate system by their direct and indirect effects, which has been extensively studied in the past few years (Andreae & Rosenfeld, 2008; Chand et al., 2009; Lohmann & Feichter, 2005; Matus et al., 2015; Rosenfeld et al., 2014; Tan et al., 2017; Ten Hoeve & Augustine, 2016). According to the most recent Intergovernmental Panel on Climate Change (IPCC) report, the radiative forcing due to aerosols from observation-based evidence was assessed to be  $-0.4 \pm 0.4 \text{ W m}^{-2}$  (IPCC, 2021). This is likely able to offset part of the warming induced by the emission of greenhouse gases (Rosenfeld et al., 2019). However, the uncertainty remains of the same order as the estimated forcing.

Whether aerosols directly warm or cool locally not only depends on aerosol physical and chemical properties, but also relies on the properties of the vertically overlapping clouds. Aerosols located above liquid clouds frequently occur off the west coast of continents as well as over the North Pacific and North Atlantic Oceans (Devasthale & Thomas, 2011). Strong reflection of liquid clouds enhances the above-cloud aerosol absorption, resulting in an increase of aerosol radiative heating rate and a change of the sign of net radiative effect at the top of atmosphere (TOA) (Chang & Christopher, 2017; Matus & L'Ecuyer, 2017; Meyer et al., 2013). For instance, biomass burning aerosols can switch from a net cooling to a net warming effect at the TOA with an increase of underlying cloud fraction (Chand et al., 2009; Keil & Haywood, 2003). Similarly, increase of underlying cloud fraction and optical depth was found to enhance the warming effect of dust aerosols (Xu et al., 2017). A cirrus layer above an aerosol layer is able to cause modest change of the radiative effect of absorbing or nonabsorbing aerosols at the TOA (Liao & Seinfeld, 1998). Considering the wide coverage of cirrus clouds and their strong regulation on the Earth's radiation (e.g., Hong & Liu, 2015; Hong et al., 2016), cirrus impact on aerosol direct radiative effect could be extraordinary, which by now has not been assessed over the globe.

Incomplete knowledge of aerosol-cloud interactions also challenges an accurate estimate of the direct radiative effect of aerosols. Cloud active aerosols interact with clouds by modifying cloud microstructure such as reducing liquid cloud effective radius (Ross et al., 2018; Tan et al., 2017), suppressing precipitation (Andreae & Rosenfeld, 2008; Rosenfeld et al., 2014), increasing cloud cover in precipitating clouds or the opposite in

non-precipitating clouds (Christensen & Stephens, 2011; Lebsack et al., 2008). These effects in turn modify aerosol direct radiative effects to an extent that depends on aerosol-cloud relative positioning in the atmosphere. Nevertheless, the fundamental understanding of aerosol-cloud-precipitation interactions and their representation in large-scale models are insufficient. For instance, IPCC AR6 reports that the total aerosol forcing including aerosol-radiation and aerosol-cloud interaction vary widely between different climate models from  $-1.50$  to  $-0.68 \text{ W m}^{-2}$  (IPCC, 2021).

Additionally, clouds modify aerosol properties. Aerosols in the vicinity of clouds were found with the lidar backscatter and extinction coefficient enhanced resulted from humidification effects on aerosol properties (Rauber et al., 2013; Su et al., 2008; Tackett & Di Girolamo, 2009; Várnai & Marshak, 2015). In contrast, aerosol loading above low-level cloud top is posited to have no significant difference with adjacent clear sky over the Southeast Atlantic according to the ORACLES (ObseRvations of Aerosols above Clouds and their intEractiOnS) field campaign data (Shinozuka et al., 2020). However, Chung et al. (2016) stated that aerosol optical depth (AOD or  $\tau_a$ ) above low-level cloud is generally smaller than those in nearby clear sky globally as showed by the CALIPSO observations. The disagreement between these two studies indicates how clouds modify aerosol properties near cloud top locally or globally may not be well understood. This lack of understanding poses challenges in reducing the uncertainties in aerosol radiative effects.

Characterizing the amount and distribution of aerosols and their co-occurrence with clouds from observations is an important step toward improving the estimate of aerosol direct and indirect effects on the Earth's climate system. Global or regional aerosol climatologies that examine aerosol loadings, seasonal variations, and land-sea contrast have been derived from passive sensors over the past couple of decades (Dey & Di Girolamo, 2010; Kim et al., 2007; Mao et al., 2014; Mehta et al., 2016; Mishchenko et al., 2007)). These climatologies represent the cloud-free aerosols and have been applied to a wide range of purposes, such as an assessment of their effects on climate (Loeb & Manalo-Smith, 2005) or model evaluation (Palacios-Peña et al., 2019). A climatology only considering the clear-sky aerosols could be biased if aerosols occurring in cloudy sky condition significantly differ from those in clear sky.

Active sensors that probe into atmosphere with cloud and aerosol vertical structures resolved are able to detect aerosols in cloudy sky under certain conditions. By utilizing the CALIPSO lidar, aerosol and cloud layers can be resolved, and a 3-D aerosol climatology has been derived in both clear and cloudy skies (Winker et al., 2013). Attention has been paid to the global distribution of the above-cloud aerosols with the help of the CALIPSO observations (e.g., Alfaro-Contreras et al., 2016; Devasthale & Thomas, 2011). There is a lack of global studies that focus on the aerosols appearing below clouds detected from space, mainly because of the concern of the lidar signal attenuation and additional uncertainty induced from the cloud layers. The CALIPSO aerosol algorithm has considered appropriate signal correction through first retrieving the overlying layers and then using the retrieved attenuation for correcting the attenuation below (Winker et al., 2009).

In this study, using the CALIPSO observations, our main objective is to characterize the properties of aerosols in clear and cloudy skies with their uncertainties considered. The distributions of cloudy aerosols are studied by considering the relative positions of cloud and aerosol layers. Overall, we focus on the following scientific questions:

1. How does the spatial distribution of aerosols occurring above, below or vertically connected to clouds differ from the cloud-free aerosols?
2. What are the optical properties and lidar parameters for the aerosols above, below or vertically connected to cloud layers and the cloud-free aerosols?
3. What are the differences in the regional and seasonal variabilities of the cloudy and the cloud-free aerosols?

## 2. Data and Methodology

### 2.1. CALIPSO

CALIPSO, launched in April 2006, carries three primary instruments: The Imaging Infrared Radiometer (IIR), the Wide Field Camera (WFC) and the near-nadir view Cloud-Aerosol Lidar with Orthogonal Polarization (CALIOP). The CALIOP operates at three channels measuring the backscatter data at 1,064 nm and the two orthogonal polarization components at 532 nm that provide near global measurements of aerosol and cloud

**Table 1**  
*Data Products and the Corresponding Variables Used in This Study*

Product	Variables
CAL_LID_L2_05kmMLay-Standard-V4-20	Column_Optical_Depth_Tropospheric_Aerosols_532 Column_Optical_Depth_Tropospheric_Aerosols_Uncertainty_532 CAD_Score Layer_Top_Altitude Layer_Base_Altitude ExtinctionQC_532 Integrated_Attenuated_Backscatter_532 Integrated_Volume_Depolarization_Ratio Final_532_Lidar_Ratio Integrated_Attenuated_Total_Color_Ratio Day_Night_Flag IGBP_Surface_Type Minimum_Laser_Energy_532 Latitude Longitude
CAL_LID_L2_05kmAPro-Standard-V4-20	Total_Backscatter_Coefficient_532

profiles (Winker et al., 2003). The CALIPSO level 2 algorithm starts from a search of atmospheric features (cloud or aerosol layers) utilizing the 532 nm attenuated backscatter profiles (Vaughan et al., 2009). The scene classification algorithm (SCA) identifies the atmospheric features as clouds (liquid or ice) or aerosols (aerosol types) (Liu et al., 2009). Profiles of extinction coefficients and particle backscatter are retrieved within the layers by the hybrid extinction retrieval algorithm (HERA) (Winker et al., 2009; Young & Vaughan, 2009). The retrieved profiles are compiling into the profile products at 5 km horizontal resolution. The vertical resolution of the profile product is 60 m below 20.2 km and 180 m above 20.2 km (Winker et al., 2003). The layer products report the layer top and base altitude, integrated optical properties, and integrated attenuated lidar backscatters. Regions with low loadings of aerosols that go undetected by CALIOP are reported as “clear air”, which are assigned a zero extinction coefficient (Winker et al., 2009).

The retrieval accuracy relies on the lidar detection threshold, the classification of aerosols and clouds, the profile calibration and the assumption of lidar ratio. The uncertainty and error sensitivity of the retrieved extinction coefficients are carefully examined in Young et al. (2013). They indicated that the assumption of lidar ratios contributes an uncertainty ranging from 30% to 50%, while overlying cirrus increases the uncertainty in the underlying layers up to 100% in some location. The aerosol retrieval uncertainty is reported in the CALIPSO products and is used in this study for additional caution for the aerosols below clouds.

The CALIPSO level 2 aerosol and cloud merged layers product, version 4-20 (CAL\_LID\_L2\_05kmMLay-Standard-V4-20) is the main data set used in this study. This merged layer product reports column properties of aerosol and cloud, including layer top and base altitude, integrated attenuated backscatter, volume depolarization ratio, color ratio, optical depth and the corresponding uncertainties calculated based on error propagation (Winker et al., 2009; Young et al., 2008, 2013). A CAD (cloud and aerosol discrimination) score is also reported for each layer, which adopts lidar backscatter, color ratio, and altitude to produce a possibility for discriminating cloud and aerosol (Liu et al., 2009, 2019). The CAD score also represents a confidence level for cloud and aerosol classification with larger absolute values for a higher confidence. The level 2 aerosol profile product (CAL\_LID\_L2\_05kmAPro-Standard-V4-20) is also used to obtain the lidar backscatter profiles at 532 nm for our climatology study. Data from 1 January 2007 to 30 June 2020 is used for this work. Table 1 summarizes the data products and variables used in this study.

One important consideration of the CALIPSO data is how to handle undetected aerosols, that is, aerosols in clear air that are below the detection threshold. With a comparison to the NASA Langley airborne High Spectral

**Table 2**

Summary of Global Mean Aerosol Optical Depth With Different Filters Applied

	All filters	No CAD filter	No Ci filter	No Ext_QC filter
Cloud-free	0.135	0.138	0.135	0.157
Cloudy	0.143	0.159	0.141	0.209
All aerosol	0.139	0.148	0.138	0.180

Resolution Lidar (HSRL), Rogers et al. (2014) evaluated the CALIPSO level 2 product, and showed significant undetected aerosols by CALIOP during daytime. Kacenelenbogen et al. (2014) found that the CALIPSO lidar only detects ~23% of the HSRL-detected above-cloud aerosols over North American. Underestimation of the aerosol occurrence by CALIOP is due to tenuous aerosol layers, which still may have significant radiative effects. For instance, using multiple years of Raman lidar observations at two sites from the Atmospheric Radiation Measurement (ARM) program, Thorsen and Fu (2015) emphasized that undetected aerosols by CALIOP cause an underestimation of aerosol direct radiative effect by 30%–50% at these two ARM sites. Also, Thorsen et al. (2017) revealed that 29% of the transparent profiles report to have zero AOD, which leads to an underestimation of aerosol direct radiative effect up to 54%. In this study, we only focus on those aerosols above the detected threshold. However, it should be kept in mind that undetected aerosols can cause some biases in the results.

## 2.2. Data Quality Control

CALIOP is experiencing low energy laser shots above the South Atlantic Anomaly (SAA) region since 2016. To exclude those low energy shots, profiles containing 532 nm laser energy less than 80 mJ are not considered as recommended by the CALIPSO team ([https://www-calipso.larc.nasa.gov/resources/calipso\\_users\\_guide/advisory/advisory\\_2018-06-12/CALIPSO\\_Laser\\_Energy\\_Technical\\_Advisory.pdf](https://www-calipso.larc.nasa.gov/resources/calipso_users_guide/advisory/advisory_2018-06-12/CALIPSO_Laser_Energy_Technical_Advisory.pdf)). Similar to Tackett et al. (2018) and Winker et al. (2013), our study also applies several filters to the CALIPSO data to ensure data quality. The data passing the filters must meet the following criteria. First, the CAD filter uses the aerosol CAD scores that must be in the range of -100 to -20, representing intermediate to high confidence levels. Second, Ext\_QC filter uses extinction\_QC\_flag\_532 values that are equal to either 0 (unconstrained retrieval; initial lidar ratio unchanged during solution process), or 1 (constrained retrieval), or 16 (opaque layers and unchanged lidar ratio), or 18 (opaque layers and changed lidar ratio). Third, the cirrus (Ci) filter identifies aerosol layers above 4 km and ensures that they are not adjacent to clouds since these may be misclassifications of cirrus fringes. Note that when a column has one aerosol layer being filtered, the whole column will be excluded in our analysis. As summarized in Table 2, aerosols in cloudy sky are influenced by the filters more than in clear sky. The Ext\_QC filter impacts the computed mean AOD more than other filters.

## 2.3. Classification of Aerosols

Figure 1 shows how we group the detected aerosol layers (i.e., those aerosols with  $\tau_a > 0$ ) for a better characterization of aerosols in cloudy sky. The quality-controlled aerosol data is divided into two main groups based on cloud presence: cloud-free and cloudy aerosols. In each cloudy sky profile, by checking the gap of the closest aerosol and cloud layers, we examine whether there are any aerosol and cloud layers that are vertically connected. If the gap is less than 0.5 km, the profile will be classified as *connected-cloud* aerosol (Figure 1b), otherwise, it will be grouped as *isolated-cloud* aerosol (Figure 1c). According to the relative vertical location of aerosol and cloud layers, the *connected-cloud* aerosols have four subcategories. When there are only one aerosol and one cloud layers in the column and they are vertically connected, this profile is classified as the *one-layer aerosol-cloud connected* group. The aerosol layer can be above or below the cloud layer. An example is shown in Figure 1b1. The second group of the connected-cloud aerosol is *aerosol-cloud connected layer below cloud layer* (Figure 1b2), where the overlying cloud can be multiple layers. *Aerosol-cloud connected layer above cloud layer* is the third group of the connected-cloud aerosol (Figure 1b3), where the underlying cloud can be multiple layers. All the connected-cloud aerosol profiles not belonging to the first three groups will be included in the four subcategories (*other connected-cloud* aerosol), including the profiles with more than one aerosol-cloud connected layers, or the profiles with multi-layer aerosols or multi-layer clouds with at least one aerosol-cloud connected layer. Figure 1d4 gives an example of the *other connected-cloud* aerosol profile. The *isolated-cloud* aerosol is grouped in a similar way. The below-cloud (Figure 1c1) aerosol can have multiple layers for the overlying clouds or the underlying aerosols. Similarly, the above-cloud aerosol (Figure 1c2) can also contain multi-layer underlying clouds or multi-layer overlying aerosols. Any profiles of the isolated-cloud aerosols that do not belong to the first two subgroups will be grouped as other isolated-cloud aerosols. Figure 1c3 gives an example.

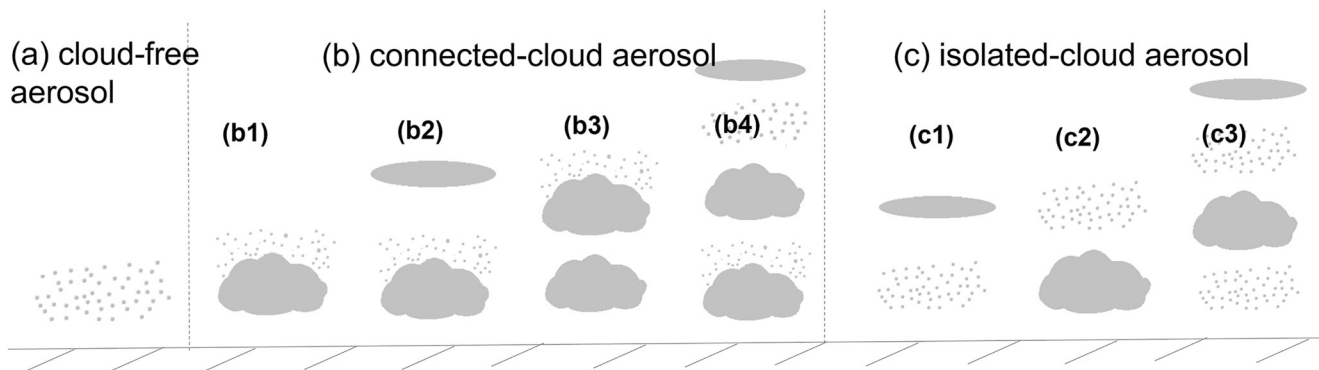


**Figure 1.** (a) Aerosol scenarios in clear sky and (b) and (c) in cloudy sky. (b) Aerosols in the column where there are at least one aerosol and cloud layers vertically connected (connected-cloud aerosol): (b1) Only one aerosol and one cloud layer in the column but vertically connected (one-layer aerosol-cloud connected), (b2) the aerosol-cloud connected layer below cloud layer, (b3) the aerosol-cloud connected layer above cloud layer, and (b4) an example for multi-layer aerosols or multi-layer clouds that do not belong to (b1–b3) (other connected-cloud aerosol). (c) Aerosols in the column where there are no aerosol and cloud layers vertically connected: (c1) Below-cloud aerosol, (c2) above-cloud aerosol, and (c3) an example for multi-layer aerosols or multi-layer clouds that do not belong to (c1–c2) (other isolated-cloud aerosol).

Figure 2 shows a CALIPSO curtain with our aerosol classification method applied to it. The shade in red indicates aerosol, while in blue indicates cloud. One can clearly see the below-cloud aerosol in the regions marked by the red dots at 20 km, the above-cloud aerosol indicated by the pink dots, and the group of the one-layer aerosol-cloud connected aerosols indicated by the green dots.

### 3. Results and Discussions

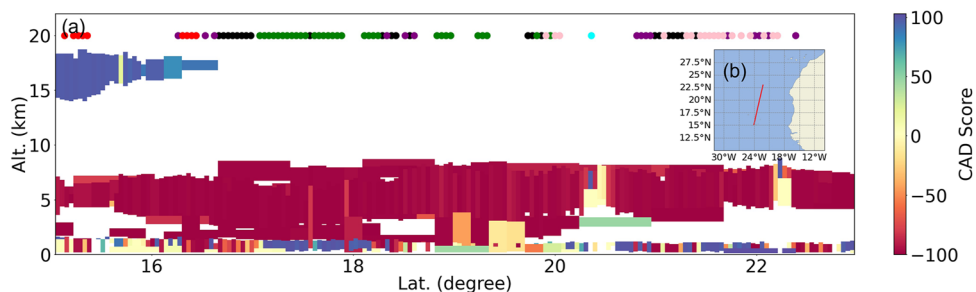
#### 3.1. Global Distributions of the Cloud-Free and the Cloudy Aerosols

Figure 3 shows the global distributions of aerosol fraction ( $f_a$ ) in clear (Figure 3a) and cloudy (Figure 3b) skies using a grid resolution of  $6^\circ$  longitude by  $5^\circ$  latitude. Aerosol fraction is defined as:

$$f_a = n_a / N_a \quad (1)$$

where  $n_a$  represents the samples for one aerosol group and  $N_a$  is the total number of aerosol samples with quality control.

As expected, the global distributions of the cloud-free and the cloudy aerosols detected by CALIOP follow the climatology of clear and cloudy skies. Specifically, in the subtropical regions, the cloud-free aerosols are dominated with  $f_a$  higher than 60%. For the cloudy aerosols,  $f_a$  values are widely spread over the tropics owing to the distribution of ubiquitous cirrus clouds (e.g., Hong & Liu, 2015; Sassen et al., 2008) and in the subtropics



**Figure 2.** (a) Cloud-aerosol groups for a case on 24 July 2019 when Cloud-Aerosol Lidar and Infrared Pathfinder Satellite Observations overpassed above the Atlantic Ocean as shown in (b). The filled circles marked at 20 km flag the aerosol classification as defined in Figure 1: Black for the cloud-free, green for the one-layer aerosol-cloud connected, blue for the aerosol-cloud connected layer below cloud layer, cyan for the aerosol-cloud connected layer above cloud layer, purple for the other connected-cloud aerosol; red for the below-cloud aerosol, pink for the above-cloud aerosols, and orange for the other isolated-cloud aerosol.

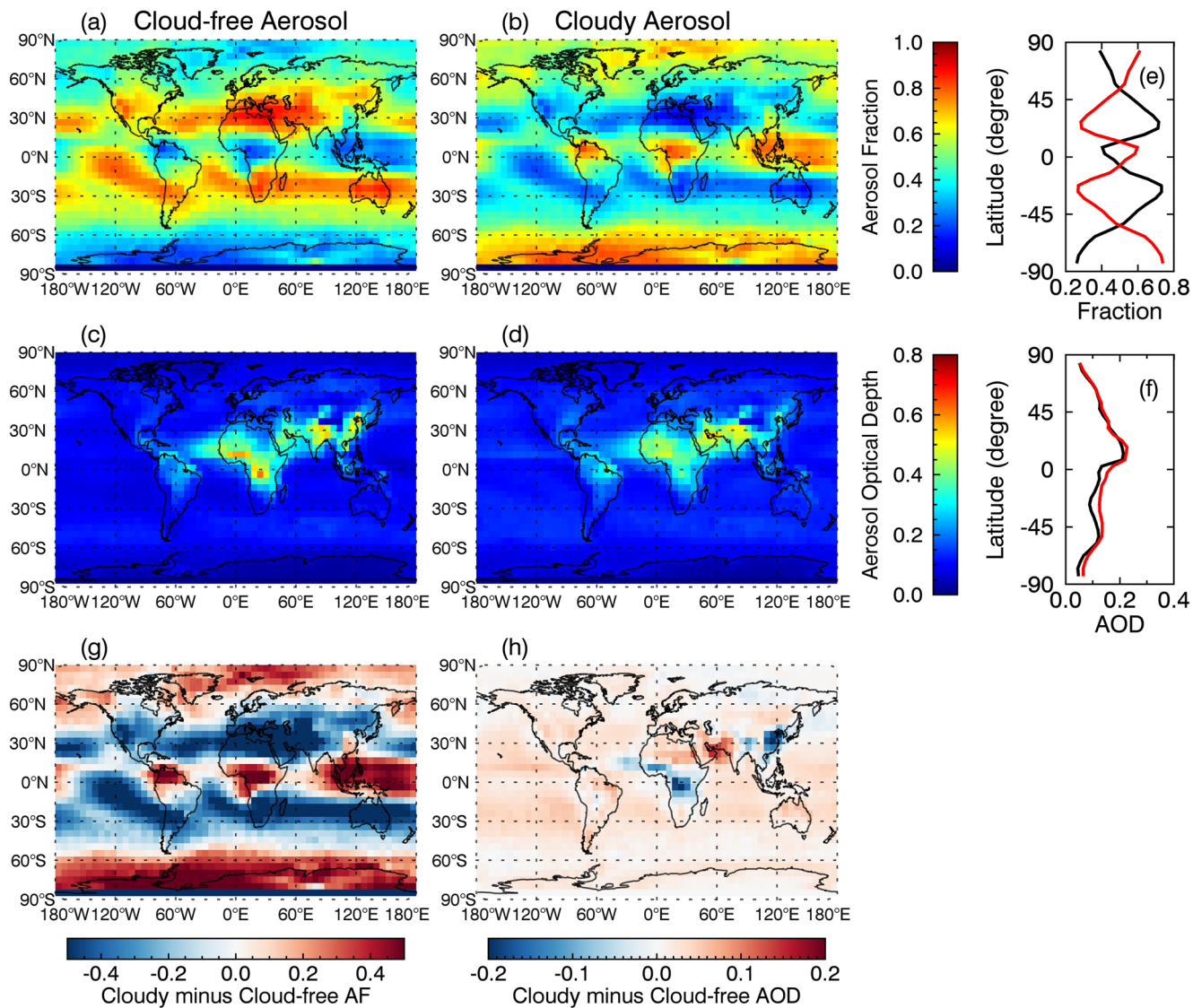


**Figure 3.** Global distributions of aerosol fraction and optical depth in cloud-free and cloudy skies are shown in (a–d). Zonal averages of aerosol fraction and optical depth are displayed in (e) and (f): Black for the cloud-free aerosol and red for the cloudy aerosols. Panel (g and h) are for the aerosol fraction and optical depth differences between the cloudy and the cloud-free aerosols.

owing to the distribution of stratocumulus clouds (e.g., Sassen & Wang, 2008). As a result, negative  $f_a$  differences (cloudy—Cloud-free) are observed over most of the subtropical regions and positive  $f_a$  differences are observed over the tropics (Figures 3e and 3g).

Mean AOD ( $\bar{\tau}_a$ ) in each  $6^\circ$  longitude by  $5^\circ$  latitude grid is calculated as the summation of optical depth divided by the total sample with  $\tau_{ai} > 0$  for each aerosol group, that is,:

$$\bar{\tau}_a = \sum_i^n \tau_{ai} / n_a \quad (2)$$

where  $\tau_{ai}$  is the optical depth of the  $i$ th aerosol sample, and  $n_a$  is the total sample for one aerosol group. Zero AOD is not included for the calculation, that is, undetected aerosols are not discussed in this study. However, it should be noted that undetected aerosols would lead to an underestimation of the mean AOD.

As shown in Figures 3c and 3d, both the cloud-free and the cloudy aerosols display relatively large values (e.g.,  $\bar{\tau}_a > 0.4$ ) over Africa, Center Atlantic Ocean, Arabian and Indian Peninsula, and East Asia. We also observe some large  $\bar{\tau}_a$  values ( $\sim 0.2$ ) over the trade wind (easterly, such as Pacific ocean) and midlatitude storm track (westerly)

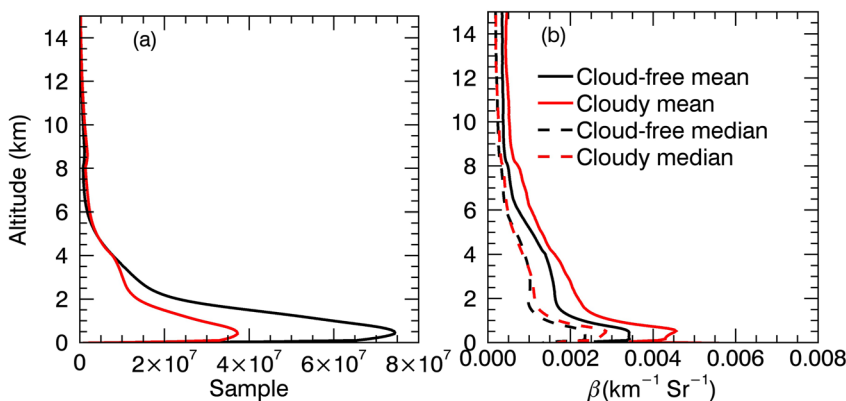


**Figure 4.** (a) Number of samples and (b) lidar backscatter profiles: Red for the cloudy aerosol, black for the cloud-free aerosol, solid line for mean values and dashed line for median values. The vertical resolution is same as level-2 aerosol profile data, that is, 60 m below 20.2 km and 180 m above 20.2 km.

regions, where sea-salt aerosols dominate the total AOD (e.g., Grythe et al., 2014). This pattern is consistent with the aerosol climatology derived from MODIS (Remer et al., 2008). The cloudy  $\bar{\tau}_a$  is generally higher over the globe, especially over Arabian Sea and its surrounding regions, whereas over the Southeast Asia and Central Africa, cloud-free  $\tau_a$  is larger (Figure 3h). Section 3.4 will show more details of the cloud-free and cloudy aerosols in different regions.

Over the globe, aerosols detected by CALIOP have about 56% samples occurring in clear sky, and another 44% occurring in cloudy sky. Cloudy aerosols occupy a smaller proportion because aerosols with low concentrations or under opaque clouds go undetected by CALIOP.

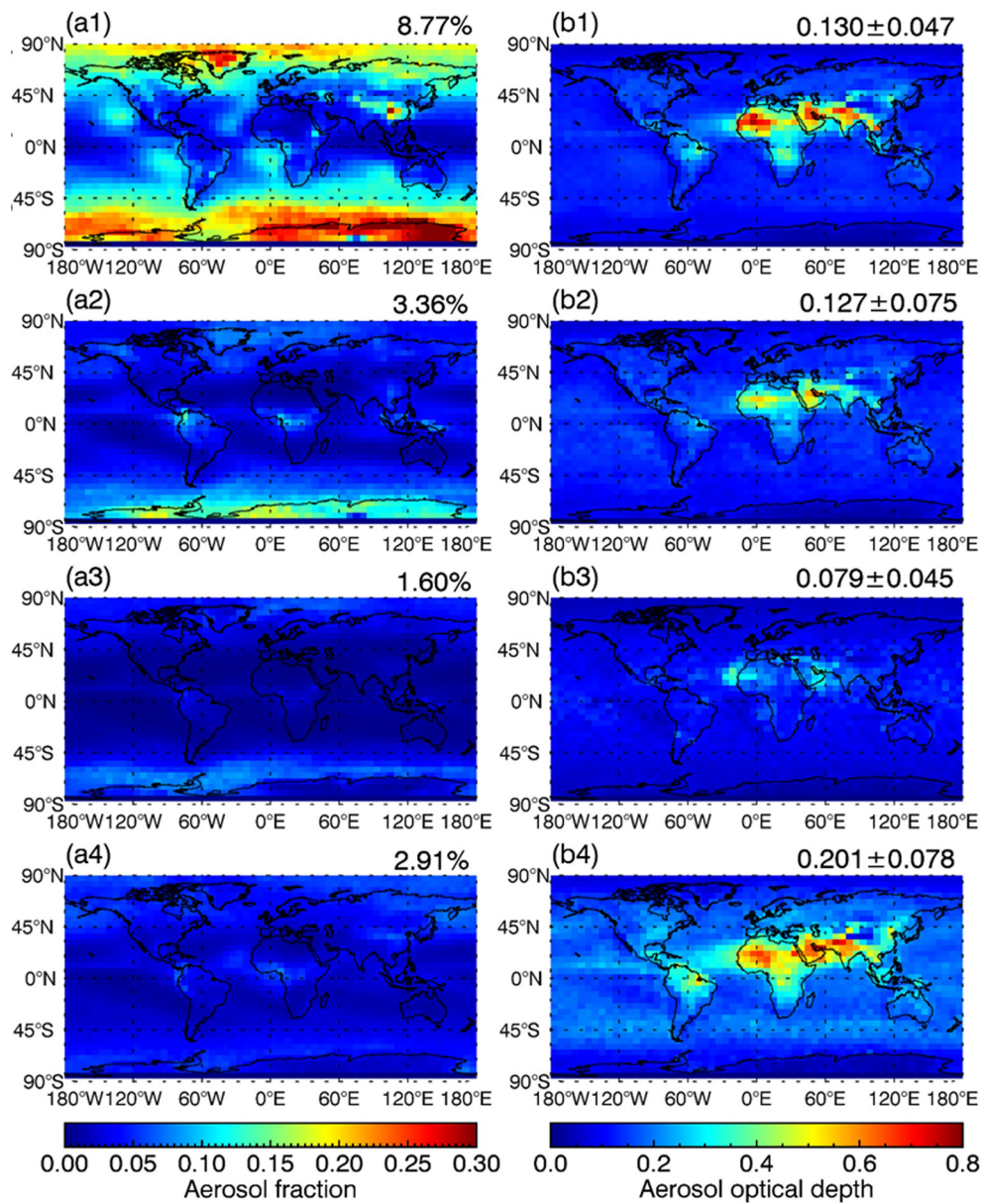
The global mean aerosol optical depth and the global mean  $\tau_a$  uncertainty for clear sky are about  $0.135 \pm 0.047$ , while in cloudy sky, they are about  $0.143 \pm 0.074$ . For all detected aerosols,  $\bar{\tau}_a$  is about  $0.139 \pm 0.059$ . An averaged  $\bar{\tau}_a$  difference of 0.008 between the cloudy and cloud-free aerosols is within the retrieval uncertainty. Here, the uncertainty reported is used the mean uncertainty calculated from the CALIPSO product, and thus represents the maximum error assuming no knowledge on how the data are correlated. Also, the mean uncertainty of the cloudy-sky aerosol is about 0.03 larger than the cloud-free aerosol, indicating bigger challenge to retrieve aerosols in cloudy sky (Winker et al., 2009).

Figure 4 displays the global profiles of detected aerosol samples and lidar backscatter ( $\beta$ ) for the cloud-free (black) and the cloudy (red) skies. As displayed, aerosols are mostly detected in the boundary layer (<2 km) with a peak occurrence at  $\sim 1$  km, and evident aerosols are also observed between 2 and 4 km. The averaged lidar backscatter profiles (solid lines in Figure 4b) show that the cloudy aerosols have stronger backscatter along all altitudes than the cloud-free aerosols. Yet the median lidar backscatter profiles show slightly stronger backscatter for the cloudy aerosols under the boundary layer. Above the boundary layer, the median lidar backscatters are quite consistent between the cloudy and the cloud-free aerosols. Larger lidar backscatter in cloudy sky agrees with larger cloudy  $\tau_a$ .

### 3.2. Global Distributions of the Connected-Cloud and the Isolated-Cloud Aerosols

To investigate the detailed characteristics of aerosols in cloudy sky, Figures 5 and 6 display the global distributions of  $f_a$  and  $\tau_a$  for the connected-cloud and the isolated-cloud aerosols.

As shown, the connected-cloud aerosols are mainly constituted by the one-layer aerosol-cloud connected and the aerosol-cloud connected layer below cloud layer groups, which account for about 8.8% and 3.4% among all aerosols detected by CALIOP, respectively (Figure 5a1 and 5a2). For the one-layer aerosol-cloud connected aerosols, relatively large  $f_a$  primarily occurs over the west of continents where marine stratocumulus prevail, including the North Atlantic ocean that is influenced by the westward transport of Sahara dust (Devasthale & Thomas, 2011; Yang et al., 2012; Zhang et al., 2016), the Southeast Atlantic that is impacted by biomass burning smoke advected from South Africa during the local winter/spring seasons (Devasthale & Thomas, 2011; Zhang et al., 2016), as



**Figure 5.** (a1–a4) Aerosol fraction and (b1–b4) optical depth for the four subgroups of the connected-cloud aerosols: First row for the one-layer aerosol-cloud connected, second row for the aerosol-cloud connected layer below cloud layer, the third row for the aerosol-cloud connected layer above cloud layer, and the bottom row for the other connected-cloud aerosol. The numbers on the upper right of each figure represent the global mean values.

well as west of North and South America, and West of Australia. Also, the one-layer aerosol-cloud connected aerosols are frequent over East Asia where low-level stratocumulus prevail during spring and winter (Hong & Di Girolamo, 2020; Klein & Hartmann, 1993), providing a high chance for clouds to be embedded in aerosol layers in the lower troposphere. For the aerosol-cloud connected layer below cloud layer group, they are primarily distributed over the tropics and midlatitude storm tracks where cirrus clouds prevail (Hong & Liu, 2015; Sassen et al., 2008). The aerosol-cloud connected layer above cloud layer and other connected-cloud aerosols account for about 1.6% and 2.9%, respectively, among all detected aerosol layers.

For optical depth, the one-layer aerosol-cloud connected (Figure 5b1) and the aerosol-cloud connected layer below cloud layer aerosols (Figure 5b2) show similar spatial patterns with those of the cloud-free aerosols. The aerosol group of the aerosol-cloud connected layer above cloud layer has the smallest  $\bar{\tau}_a$  (Figure 5b3), while the

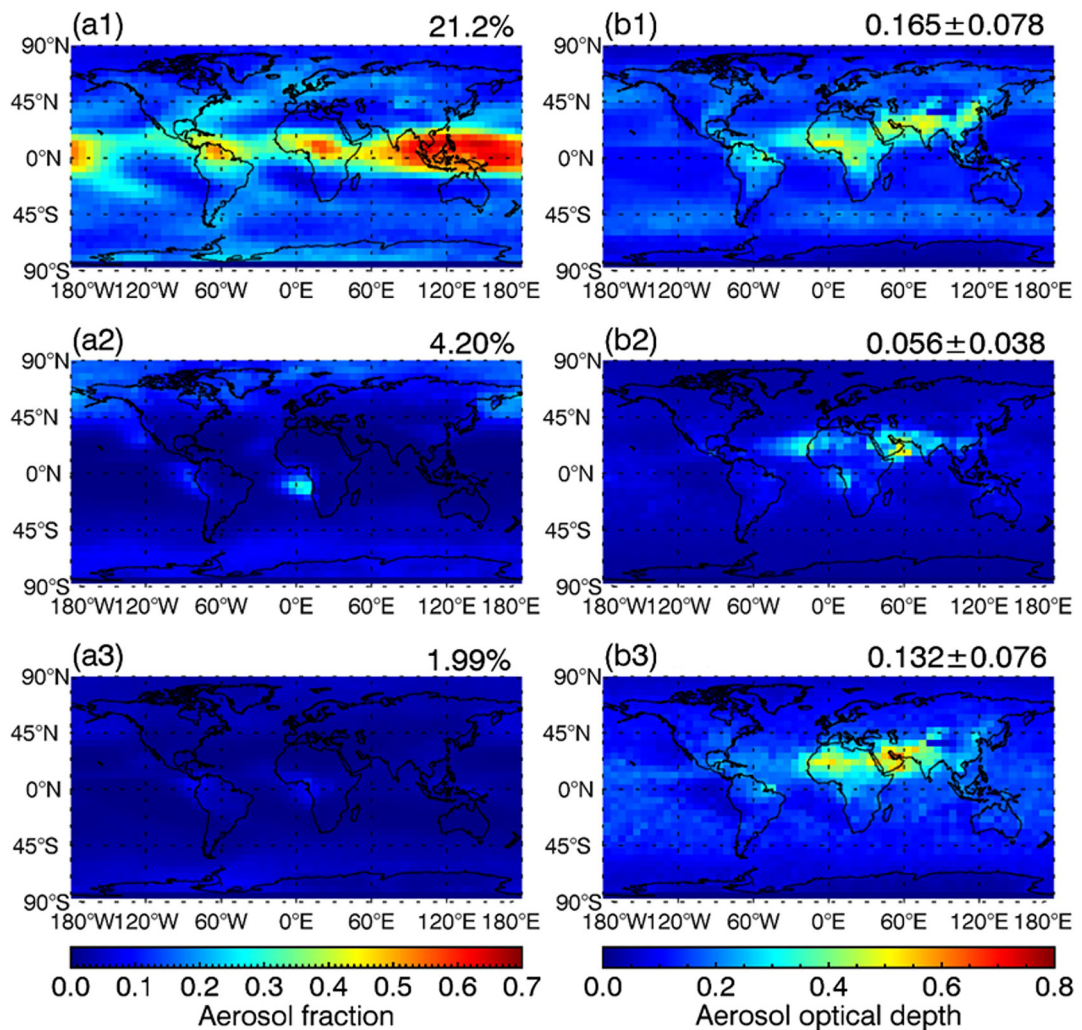


**Figure 6.** Same as Figure 5 but for the isolated-cloud aerosol: The upper panels for the below-cloud aerosol, the middle panels for the above-cloud aerosol, and the lower panels for the other isolated-cloud aerosol. The numbers on the upper right of each figure represent the global mean values.

other connected-cloud aerosols have the largest  $\bar{\tau}_a$ , particularly over ocean and over the “dust belt” across the Sahara and eastward to Arabia and Southwest of Asia (Figure 5b4). Also, the aerosol-cloud connected layer below cloud layer (Figure 5b2) and the other connected-cloud aerosols (Figure 5b4) have larger  $\tau_a$  uncertainties than the other two connected-cloud aerosol groups, that is, the one-layer aerosol-cloud connected (Figure 5b1) and the aerosol-cloud connected layer above cloud layer (Figure 5b3). The overlying clouds induce additional uncertainty to the lower aerosol layers as discussed in Sections 1 and 2.1 (Winker et al., 2009; Young et al., 2013).

Figure 6 shows the distributions of the isolated-cloud aerosols. The below-cloud aerosols (Figure 6a1) account for about 21.2% among all aerosols, occurring frequently in the tropics where ubiquitous cirrus clouds occur (Hong & Liu, 2015; Sassen et al., 2008). The fraction of the above-cloud aerosols (Figure 6a2) are about 4%, and are primarily distributed over ocean, that is, west of Africa and America, as well as east of Asia, agreeing with the results from previous research that focused on the above-cloud aerosols (Devasthale & Thomas, 2011; Yang et al., 2012; Zhang et al., 2016). For the other isolated-cloud aerosols (Figure 6a3), their global average fraction is about 2%. The  $\bar{\tau}_a \sim 0.165$  of the below-cloud aerosols is larger than that of the cloud-free aerosols ( $\bar{\tau}_a \sim 0.135$ ). The above-cloud aerosols have smaller  $\bar{\tau}_a$  (0.056) than the cloud-free aerosols primarily due to a shallower integrated column than the cloud-free aerosols. Also, the mean aerosol optical depth uncertainties of the below-cloud and other isolated-cloud groups tend to be larger than the cloud-free or the above-cloud aerosols. The retrieved

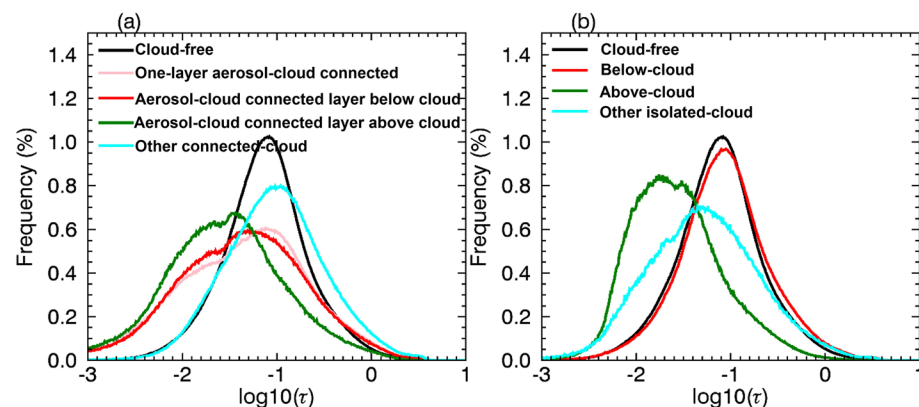


**Figure 7.** The probability distribution functions of aerosol optical depth for global aerosols: (a) The connected-cloud aerosols and (b) the isolated-cloud aerosols with a contrast to the cloud-free aerosols shown in the black curve in both (a and b).

cloud attenuation used for the underlying layer signal correction is responsible for the additional uncertainty to aerosol layers (Chung et al., 2016; Winker et al., 2009).

It has been noted that the cloudy aerosols are primarily occupied by the below-cloud aerosols ( $\bar{f}_a \sim 21.2\%$ ), which account for almost half of the detected cloudy aerosols ( $\bar{f}_a \sim 44\%$ ). Considering that tenuous aerosols and aerosols under opaque clouds are missed by CALIOP, the below-cloud aerosols are more spread than what we observe from Figure 6a1. Liao and Seinfeld (1998) stated that a cirrus cloud layer causes modest changes of aerosol radiative effect at TOA about  $1 \text{ W m}^{-2}$  change compared to no cirrus presence based on radiative transfer simulations. The wide coverage and frequent occurrence of the below-cloud aerosols indicates that the impact of cirrus to aerosol direct radiative effect could be significant over the globe.

It is also noted that the mean  $\tau_a$  uncertainties are larger for those aerosols with overlying cloud layers in the column, that is, the aerosol-cloud connected layer below cloud layer and below-cloud aerosols, compared to the situations without overlying cloud presence, that is, the one-layer aerosol-cloud connected and the cloud-free aerosols. In Section 3.3, we further examine the  $\tau_a$  distributions and other aerosol properties to investigate whether there is any similarity between aerosols with and without overlying cloud layers.

### 3.3. Optical Property and Lidar Variables

#### 3.3.1. Optical Depth

The probability density functions (PDF) of  $\tau_a$  are shown in Figure 7 for the cloud-free, the connected-cloud and the isolated-cloud aerosols. The cloud-free  $\tau_a$  PDF is nearly a lognormal distribution with a peak at  $\tau_a \sim 0.083$  (Table 3). For the connected-cloud aerosols, their PDFs are generally wider than the cloud-free aerosols

and have higher frequencies at small  $\tau_a$  regions. The one-layer aerosol-cloud connected and the aerosol-cloud connected layer below cloud layer aerosols show close PDFs (Figure 7a, pink and red), close values in their means, modes and medians (Table 3b1 and 3b2) with a comparison with other aerosol groups. The PDF of the aerosol-cloud connected layer above cloud layer aerosols (Figure 7a, green) shows much higher frequency for  $\tau_a < \sim 0.04$ . This group of aerosols have the smallest mean, mode and median values among all the connected-cloud aerosol groups.

Similarly, for the isolated-cloud aerosols, the below-cloud aerosols show a very close PDF with the cloud-free aerosols but with slightly larger mode ( $\sim 0.089$ ), median and mean values (Table 3c1). In contrast, the above-cloud aerosols have much smaller mode values than the cloud-clear aerosols as shallower aerosol columns contribute to a smaller  $\tau_a$ .

**Table 3**

*The Aerosol Optical Depth Medians, Modes and Means for the Cloud-Free, the Connected-Cloud and the Isolated-Cloud Aerosols*

Cloud-free	Connected-cloud				Isolated-cloud			
	b1	b2	b3	b4	c1	c2	c3	
Median	0.076	0.048	0.043	0.027	0.093	0.083	0.024	0.050
Mode	0.083	0.075	0.052	0.038	0.110	0.089	0.017	0.048
Mean	0.135	0.130	0.127	0.079	0.201	0.165	0.056	0.132

*Note.* b1–b4 and c1–c4 represent the same aerosol categories as Figure 1b1–1b4 and Figure 1c1–1c3, Respectively.

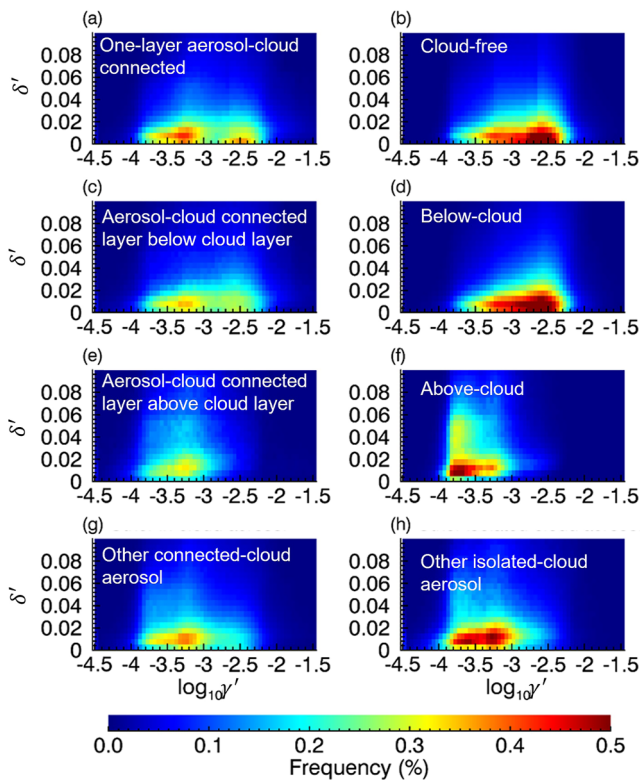


**Figure 8.** Two-dimensional histogram of the integrated attenuated lidar backscatter (in  $\log_{10}$  scale) versus depolarization ratio for the cloud-free, the connected-cloud and the isolated-cloud aerosols. The total frequency of each diagram is equal to 100.

### 3.3.2. Depolarization Ratio and Lidar Backscatter

The integrated attenuated backscatter ( $\gamma'$ ) and depolarization ratio ( $\delta'$ ) are two important variables for constraining aerosol type selections (Omar et al., 2009). Figure 8 shows the two-dimensional (2-D) histogram of  $\gamma'$  versus  $\delta'$  for the detected aerosol layers, integrated from layer base to top. As displayed, most of the one-layer aerosol-cloud connected (Figure 8a), the aerosol-cloud connected layer below cloud layer (Figure 8c), the cloud-free (Figure 8b), and the below-cloud aerosols (Figure 8d) have  $\delta < 0.02$ . In contrast, the aerosol-cloud connected layer above cloud layer (Figure 8e) and the above-cloud aerosols (Figure 8f) show tremendous samples with  $\delta > 0.02$ . These two groups of aerosols distribute in the regions where dust and biomass burning aerosols frequently occur (Figures 5a3 and 6a2), being consistent with relatively large  $\delta$  indicating desert dust and biomass burning aerosols (Burton et al., 2012; Omar et al., 2009). Moreover, the connected-cloud aerosols tend to have the integrated attenuated lidar backscatter less than  $0.001 \text{ Sr}^{-1} \text{ km}^{-1}$ , agreeing with higher frequency of small  $\tau_a$  in Figure 7a. For the cloud-free and the below-cloud aerosols, they have most samples with  $\gamma' > 0.001 \text{ Sr}^{-1} \text{ km}^{-1}$ , indicating marine and polluted continental aerosols (Omar et al., 2009). The above-cloud aerosols rarely have  $\gamma' > 0.001 \text{ Sr}^{-1} \text{ km}^{-1}$ . Again, the cloud-free and the below-cloud aerosols share similar  $\gamma'-\delta'$  diagram with the samples concentrated in the regions of  $\gamma' > 0.001 \text{ Sr}^{-1} \text{ km}^{-1}$  and  $\delta' < 0.02$ . It is also similar for the one-layer aerosol-cloud connected and the aerosol-cloud connected layer below cloud layer aerosols, which have a similar pattern in  $\gamma'-\delta'$  diagram with the samples concentrated in two regions: (a)  $\gamma' \sim 0.0003\text{--}0.001 \text{ Sr}^{-1} \text{ km}^{-1}$  and  $\delta' < 0.02$  and (b)  $\gamma' \sim 0.003 \text{ Sr}^{-1} \text{ km}^{-1}$  and  $\delta' < 0.02$ .

### 3.3.3. Lidar Ratio and Color Ratio

The lidar ratio for aerosol ( $S_a$ ), that is, the extinction coefficient to lidar backscatter ratio, is essential to obtain aerosol optical depth. The CALIPSO aerosol type classification assigns one  $S_a$  to one aerosol type (Omar et al., 2009). In the V4 data, lidar ratio has been updated to better represent aerosol types (Kim et al., 2018). Six main aerosol types are shown in Figure 9, that is, clean marine ( $S_a = 23 \text{ sr}$ ), dusty marine ( $S_a = 37 \text{ sr}$ ), dust/volcanic ash ( $S_a = 44 \text{ sr}$ ), clean continental ( $S_a = 53 \text{ sr}$ ), polluted dust ( $S_a = 55 \text{ sr}$ ) and polluted continental/smoke/elevated smoke ( $S_a = 70 \text{ sr}$ ) aerosol. The dots and error bars in Figure 9 represent means and standard deviations of the layer-integrated attenuated total color ratio ( $\chi'$ ) for each aerosol type. The number near each aerosol type is obtained by integrating the frequency over the y axis, that is, the color ratio, representing the proportion of each aerosol type within that aerosol group. For instance, Figure 9b shows that the cloud-free aerosols contain about 45.9% samples being classified as clean marine aerosols.

The proportions of aerosol types in each aerosol group are closely related to aerosol distributions over the globe. Clean marine aerosols are the primary aerosol type for the cloud-free (Figure 9b, 45.9%), the one-layer aerosol-cloud connected (Figure 9a, 36.5%), the aerosol-cloud connected layer below cloud layer (Figure 9c, 32.5%) and the below-cloud (Figure 9d, 49.8%) aerosols. In particular, the below-cloud aerosols show a similar  $S_a-\chi'$  pattern with the cloud-free aerosols. The cloud-free aerosol group is slightly larger in the proportions of dust/volcanic ash and polluted dust aerosols, while the below-cloud aerosol group is about 4% and 1.3% higher in clean marine and dusty marine aerosols. For the above-cloud (Figure 9f) and the aerosol-cloud connected layer above cloud layer aerosols (Figure 9e), they share similar aerosol types as well. Dust/volcanic ash (>30%), polluted dust (~24%) and elevated smoke (~25%) are the three dominated aerosol types, but the clean marine or dusty marine aerosols are rare (<5%) for these two aerosol groups. The mean and standard deviation of the color ratio between the cloud-free and the below-cloud aerosols are similar with a mean color ratio of about 0.5 for clean

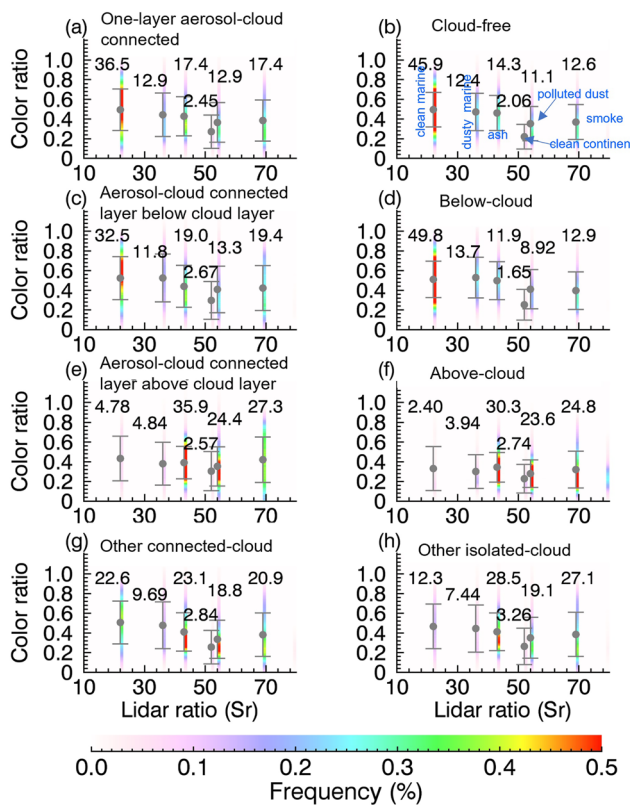


**Figure 9.** Two-dimensional histograms of lidar ratio versus color ratio. The gray dots and error bars represent the mean and standard deviation of color ratio, while the number represents the total fraction of each aerosol type.

marine, dusty marine and dust/volcanic ash aerosols, about 0.4 for polluted dust and polluted continental/smoke/elevated smoke, and about 0.2 for clean continental aerosols.

Overall, the  $\tau_a$  distributions, the  $S_a - \chi'$  and  $\gamma' - \delta'$  diagrams have shown similarity between the one-layer aerosol-cloud connected and the aerosol-cloud connected layer below cloud layer aerosols as well as between the cloud-free and the below-cloud aerosols. Some differences in these properties between aerosols with and without overlying clouds could result from their contrast in spatial distributions as discussed in Section 3.2, from the accuracy of cloud-aerosol discrimination, from additional uncertainties induced by the overlying cloud layers as well as from a modification of aerosol properties by cloud layers.

### 3.4. Regional and Seasonal Analysis

As displayed in Section 3.2, aerosols are unevenly distributed over the globe. To characterize the regional aerosol variability, we show aerosol properties in cloudy and clear skies for nine selected locations shown in Figure 10. These regions are chosen because they are known to be significantly affected by anthropogenic and natural activities. Figures 11 and 12 display the timeseries of monthly  $f_a$  and  $\bar{\tau}_a$  for the cloud-free (red), the cloudy (orange, a combination of the connected-cloud and the isolated-cloud), the connected-cloud (green), the isolated-cloud (gray) aerosols. Figures 13 and 14 show the profiles of aerosol samples and median lidar backscatters.

For the whole globe, the cloudy and the cloud-free  $\bar{\tau}_a$  values show seasonal variations ranging roughly from 0.1 to 0.15, being larger during boreal summer and smaller during boreal winter (Figure 12a). The seasonal variations agree with results from passive sensor measurements such as MODIS and MISR (Mehta et al., 2016; Mishchenko et al., 2007; Remer et al., 2008). In contrast, the cloud-free and cloudy aerosol fractions are quite flat (Figure 11a).

In different regions, the variations of  $\bar{\tau}_a$  and  $f_a$  differ significantly between the cloud-free and the cloudy aerosols, which rely on the variations of cloud systems, local emissions, and long-range transport. For example, in the Malaysia-Indonesia regions (Figures 11–14i), the fraction of aerosols in cloudy sky, primarily contributed by the below-cloud aerosols (Figure 6a), is two times more than that of the cloud-free aerosols due to the ubiquitous

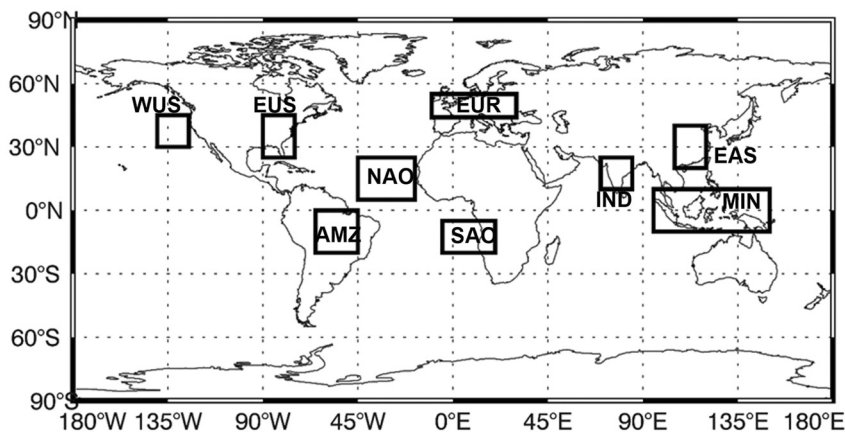


**Figure 10.** Selected areas for studying the seasonal variations of aerosol fraction and optical depth derived from Cloud-Aerosol Lidar with Orthogonal Polarization: EAS short for East Asian region, MIN for Malaysian-Indonesia region, IND for Indian region, EUR for European region, NAO for North Atlantic Ocean, SAO for Southeast Atlantic Ocean, EUS for East US, WUS for west of US, AMZ for Amazonian region.

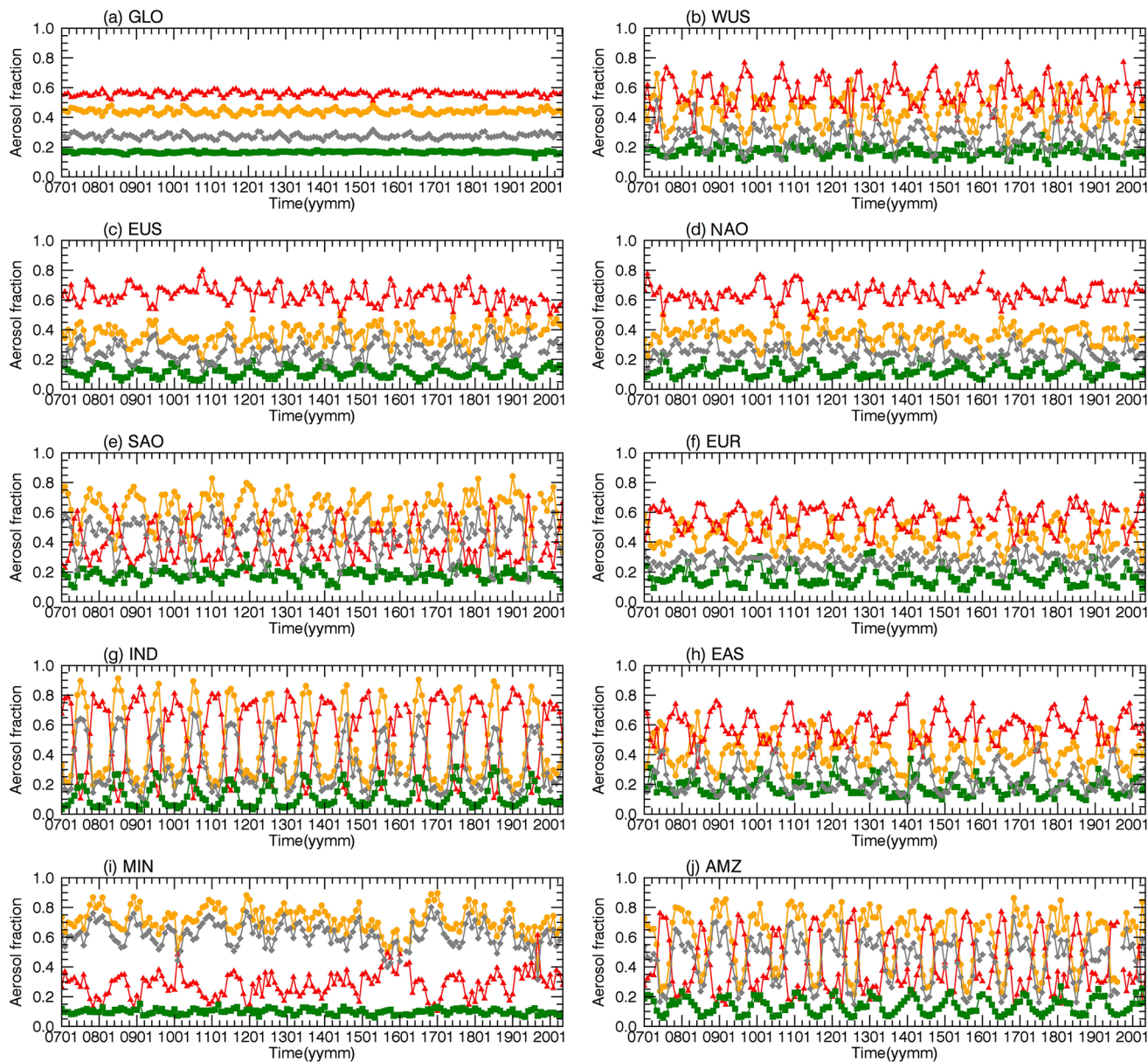


**Figure 11.** The timeseries of aerosol fraction for the selected regions as displayed in Figure 10: Red—the cloud-free aerosol, orange—the cloudy aerosol, green—The connected-cloud aerosol, gray—the isolated-cloud aerosol.

cirrus in this region (Figure 11i). The cloudy  $\bar{\tau}_a$  is slightly larger than the cloud-free  $\bar{\tau}_a$ , while the connected-cloud  $\bar{\tau}_a$  is the largest in this region (Figure 12i). The climate impact in this region is observable—The cloud-free aerosols account for a higher fraction during the winter-spring seasons of 2009–2010, 2015–2016 and 2019–2020 when El Niño phase dominated; during the La Niña years such as 2010, 2017 and 2018, cloudy aerosols have larger fractions. The detected aerosols primarily occur below 4 km (Figure 13i). The median backscatter profiles (Figure 14i) also show that the connected-cloud aerosols tend to have the largest backscatter, extending up to 4 km. The isolated-cloud and the cloud-free aerosols have their median backscatter profiles nearly overlapped below 4 km, indicating the similarity between aerosols with and without overlying clouds.

In the Southeast Atlantic region, aerosols are frequently transported above stratocumulus during the biomass burning season (local winter) (Zhang et al., 2016). The cloudy aerosols account for up to 80% among all aerosols during local summer and are primarily contributed by the isolated-cloud (above-cloud) aerosols. The cloud-free aerosols show that  $\bar{f}_a$  peaks in May–August with fraction up to 60%.  $\bar{\tau}_a$  in this region is larger in local winter

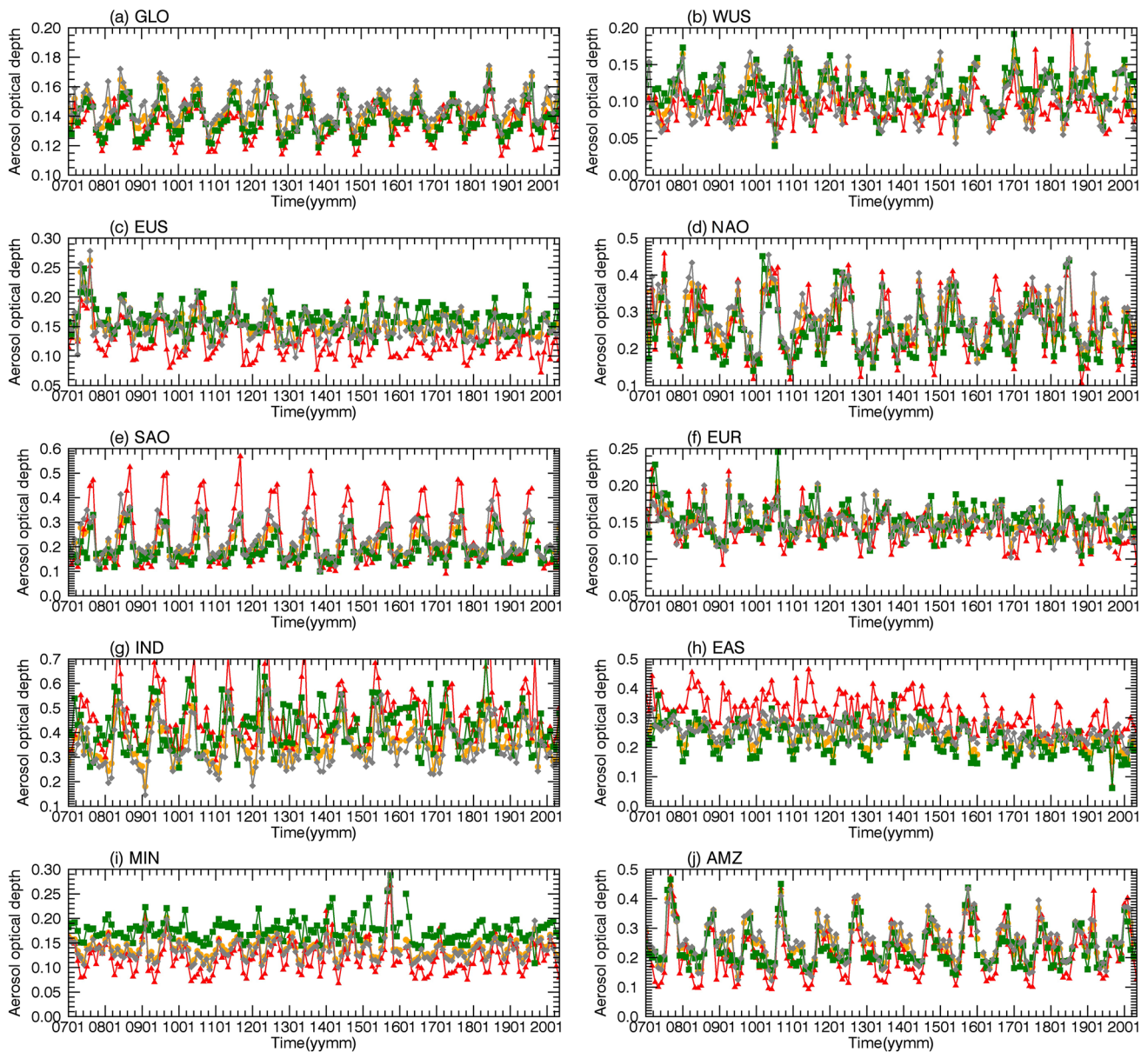


**Figure 12.** Same as Figure 11 but for the timeseries of aerosol optical depth.

due to biomass aerosols and smaller during summer (Figure 12e). The connected-cloud and the isolated-cloud  $\tau_a$  are smaller than the cloud-free aerosols in this region because aerosols are frequently transported above stratus cumulus so that cloudy  $\tau_a$  is integrated over a shallower column compared to clear sky. This is also revealed in Figure 13e that shows a peak located at  $\sim 3$  km, that is, above boundary layer, and another peak in the boundary layer ( $\sim 1$  km). It is obvious that there are two bumps in the median backscatter profiles (Figure 14e)—One below 1 km and another one between 2 and 6 km, contributing by the boundary-layer and the elevated aerosols, respectively.

Similarly, over the North Atlantic Ocean region (Figures 11–14d), aerosols originating from African dust are often elevated and transported westward (Yang et al., 2012). As displayed in Figures 13d and 14d, aerosols are concentrated in the boundary layer below 2 km but with another peak between 2 and 6 km. In this region, the cloud-free aerosols account for more than 50% through the year with no obvious seasonal cycles. However, the connected-cloud aerosol fraction displays seasonal periodicity that relates to the cumulus which appear from March – August each year (Figure 11d; King et al., 2013). The timeseries of both the cloud-free and cloudy  $\bar{\tau}_a$

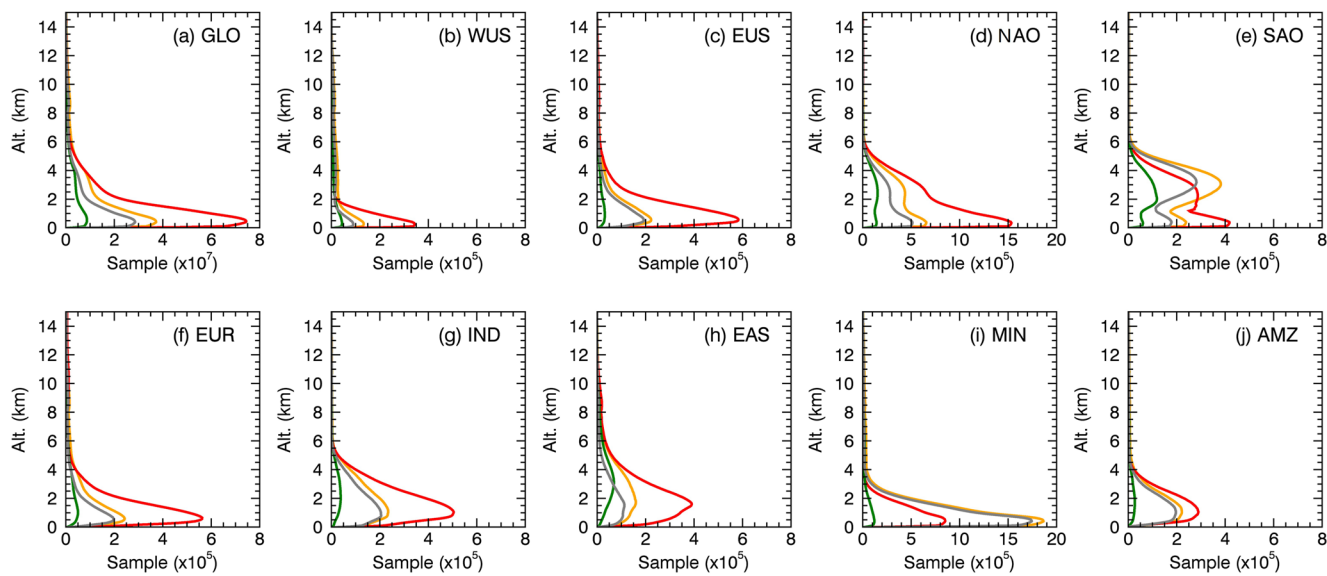


**Figure 13.** Same as Figure 11 but for vertical profiles of samples.

overlaps well, being larger in boreal summer season (Figure 12d) due to the outbreak of Saharan air layer (Xian et al., 2020).

In the East Asian and Indian regions, aerosol characteristics are impacted by the Asian monsoon. The cloud-free aerosols constitute a higher fraction than the cloudy aerosols during the winter monsoon season in both regions, and vice versa during the summer monsoon season (Figures 11g and 11h). In the Indian region,  $\bar{\tau}_a$  peaks in summer as the prevailing Southwest surface wind transports dust particles from the desert from Asia and Africa to India and its surrounding regions (Dey & Di Girolamo, 2010; Sivaprasad & Babu, 2014). The cloud-free  $\bar{\tau}_a$  is generally larger than the connected-cloud  $\bar{\tau}_a$ , while the isolated-cloud  $\bar{\tau}_a$  is the smallest (Figure 12g). In East Asia, the connected-cloud aerosols are more prevalent during winter-spring season due to the prevalence of low stratiform clouds (Hong & Di Girolamo, 2020; Klein & Hartmann, 1993), while the isolated-cloud aerosols (primary below-cloud aerosol) are being more frequent during the summer monsoon (Figure 11h). Similar to Indian region, the cloud-free  $\bar{\tau}_a$  is larger than the cloudy  $\bar{\tau}_a$  as well, with the connected-cloud  $\bar{\tau}_a$  being the smallest. In both

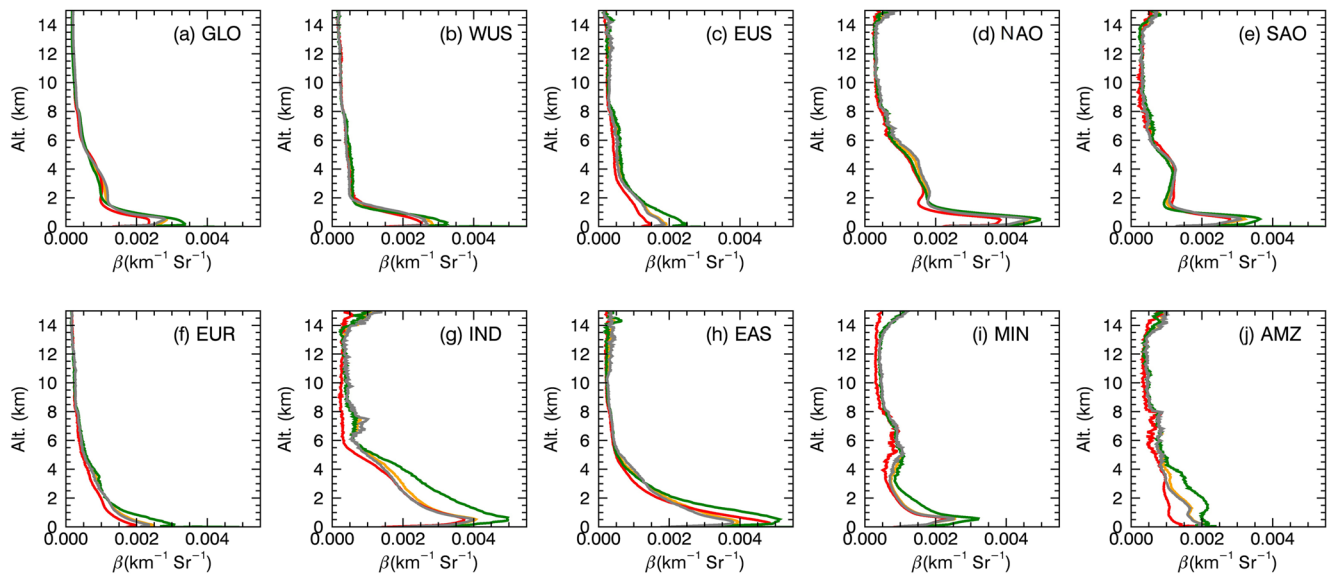


**Figure 14.** Same as Figure 11 but for profiles of the median values of lidar backscatters at 532 nm.

regions, aerosols are detected up to 6 km (Figures 13g and 13h), whereas in India, aerosol backscatters are large up to 6 km and in East Asia, they decrease substantially above 2 km (Figures 14g and 14h).

In the other four regions- Europe (Figures 11f–14f), west of US (Figures 11b–14b), east US (Figures 11c–14c) and Amazon (Figures 11j–14j), the seasonal variations and the behaviors of the cloud-free and the cloudy aerosols also heavily rely on local weather and climate. For instance, in the Amazonian regions, the  $\bar{\tau}_a$  and  $\bar{f}_a$  peak in the dry season, and cloudy aerosols are dominated by the below-cloud aerosols (>40%, Figure 6) due to ubiquitous cirrus. In west of US, seasonal variation of the cloudy aerosols is also associated with the seasonal cycle of stratocumulus, which is more abundant in summer (Klein & Hartmann, 1993). Also, smoke aerosols from frequent wildfire events over west coast of North America would be transported above the stratocumulus decks (Mallet et al., 2017; Schulze et al., 2020) that modify the seasonal variations of AOD. Aerosols in west of US are detected below 2 km and rare aerosols are elevated above boundary layer. In Europe, east US and Amazon, aerosols can be detected up to 4 km due to a deeper mixing-layer height.

Overall, the characteristics of the cloud-free and the cloudy aerosols as well as their seasonal variations significantly vary with regions. In some regions such as in East Asia, the cloud-free  $\bar{\tau}_a$  tends to be the largest, while in some other regions such as in Malaysia-Indonesia region, the cloud-free  $\bar{\tau}_a$  is the smallest. The difference in the cloudy and the cloud-free  $\bar{\tau}_a$  in a region relies on their differences in aerosol types, geometrical thickness of the aerosol layers as well as the retrieved  $\tau_a$  uncertainties. It should be noted that the geometrical thickness of aerosol layers is overall larger in clear sky than in cloudy sky, which should result in larger cloud-free  $\bar{\tau}_a$ . However, aerosol-cloud interactions and larger  $\tau_a$  uncertainties in cloudy sky could also contribute to a larger cloudy  $\bar{\tau}_a$ . To what degree is contributed by aerosol-cloud interaction to  $\tau_a$  is not inferred in this study.

Regardless of regional  $\tau_a$  differences, there are some common features. The median lidar backscatter profiles of the cloudy and the cloud-free aerosols are nearly identical in all regions. However, the connected-cloud median backscatter profiles are the largest among all aerosol groups for all regions. The larger lidar backscatter of the connected-cloud aerosols could result from an enhancement of aerosol backscatter near cloud edge (e.g., Tackett & Di Girolamo, 2009). Misclassification of clouds, especially cloud detrainments near cloud boundary, as aerosols likely induces larger lidar backscatters to the connected-cloud aerosols as well.

#### 4. Summary

This study examines the climatological properties of aerosols detected by CALIOP occurring in cloud-free and cloudy skies. Considering that clouds above or below aerosol layers influence aerosol direct radiative effects in different ways, cloudy aerosols are further classified into the connected-cloud and the isolated-cloud aerosols based on the relative vertical locations of aerosol and cloud layers. The differences between the cloud-free and the cloudy aerosols are emphasized by examining their spatial distributions, optical property, seasonal and regional variations.

Overall, for all the detected aerosols by CALIOP that pass our quality filters, the cloud-free aerosol samples account for about 55.9%, and the cloudy aerosol samples occupy about 44.1% over the globe. The cloudy aerosol samples are underestimated as CALIOP misses very thin aerosols and aerosols under opaque clouds. The global average optical depth ( $\bar{\tau}_a$ ) and mean uncertainty of the cloud-free and the cloudy aerosols are  $0.135 \pm 0.047$  and  $0.143 \pm 0.074$ , respectively. The connected-cloud aerosols, occurring frequently in the marine stratocumulus and East Asian regions, have a  $\bar{\tau}_a \sim 0.138 \pm 0.063$ . The below-cloud aerosols, frequently occurring in the regions covered by ubiquitous cirrus, have a  $\bar{\tau}_a \sim 0.165 \pm 0.087$ , whereas the above-cloud aerosols tend to have smaller  $\bar{\tau}_a \sim 0.056 \pm 0.039$ .

The cloud-free, the below-cloud, the one-layer aerosol-cloud connected and the aerosol-cloud connected layer below cloud layer aerosols primarily consist of marine aerosols, while the aerosol-cloud connected layer above cloud layer and the above-cloud aerosols contain more elevated smoke, polluted dust and volcano ash aerosols. We find similar  $\tau_a$  PDFs,  $\gamma' - \sigma'$  and  $S_a - \chi'$  diagrams between the one-layer aerosol-cloud connected and the aerosol-cloud connected layer below cloud layer aerosols, as well as between the below-cloud and the cloud-free aerosols. These similarities may indicate that clear sky aerosol climatologies from passive sensors may well be globally representative of all-sky conditions. However, considering the additional uncertainties caused by the overlying cloud layers to the underlying aerosols observed from space-borne lidar, it is necessary to utilize

ground-based lidar observations to confirm the similarity of aerosol properties with and without cloud layers above.

Also, this study reveals a wide coverage of the below-cloud aerosols that are frequently distributed over the tropical regions, which account for about ~21.2% among all the detected aerosols. Due to the fact that a cirrus layer is able to modify aerosol direct radiative effect at the TOA and heating rates in the atmosphere, it is important to quantify the degree to which of cirrus clouds change the underlying aerosol direct effect in order to obtain an accurate estimate of the role of aerosols in Earth's radiation budget. The ground-based observations such as from the ARM program provide important measurements of clouds, aerosols and radiation that will serve for simulating and constraining regional aerosol direct radiative effect at the TOA in both clear and cloudy skies as demonstrated in two recent studies (Balmes & Fu, 2021; Wu et al., 2021).

Our results also suggest that regional and seasonal variations of the cloud-free and the cloudy aerosol fraction and optical depth are strong, which are affected by local emissions and seasonal variability of regional climates. In East Asia and Southeast Atlantic Ocean, the cloud-free  $\bar{\tau}_a$  is the largest, and the connected-cloud  $\bar{\tau}_a$  is the smallest, vice versa in East US, West US and Malaysia-Indonesia regions. The connected-cloud lidar backscatter profiles (median values) are the largest among different aerosol groups in all selected regions. As aerosol and cloud layers are vertically connected, aerosol properties can be affected by clouds. Hygroscopic aerosols might grow in a more humid environment near clouds (e.g., Rauber et al., 2013). Detrainment, entrainment and cloud processes could also alter aerosol properties. Also, small cloud segments near cloud boundary also pose challenges for the aerosol-cloud discrimination, leading to some cloudy pixels being identified as aerosols. To what degree the cloud contamination contributes to the connected-cloud profile is unknown.

Finally, while this study has provided a comprehensive analysis of the cloud-free and the cloudy aerosols, it is incomplete. CALIOP does not detect all radiatively significant aerosols as discussed in previous studies (Kacenelenbogen et al., 2014; Rogers et al., 2014; Thorsen & Fu, 2015; Thorsen et al., 2017). Therefore, airborne or ground-based lidar observations continue to be important in assessing aerosol direct radiative effect in both clear and cloudy skies. For example, the CAMP<sup>2</sup>Ex (Cloud and Aerosol Monsoonal Processes Philippines Experiment) field campaign that took place in 2019 has provided comprehensive measurements in cloud, aerosol and radiation over the Philippines and its surrounding regions (Di Girolamo et al., 2018). This field campaign provides an unprecedented opportunity to investigate aerosols below cirrus clouds and to quantify the cirrus' impact on aerosol direct radiative effects. The future Atmospheric Observing System (AOS) mission with an HSRL onboard will also provide better global measurements of aerosols including those that are optically thin. The biases of aerosol properties in cloudy sky are expected to be reduced by future spaceborne lidar measurements that are more advanced than CALIOP.

## Data Availability Statement

Data -The Cloud-Aerosol Lidar and Infrared Pathfinder Satellite Observations data can be directly downloaded from the NASA Langley Research Center Atmospheric Science Data Center (NASA/LARC/SD/ASDC., 2018b; 2018a), available at <https://asdc.larc.nasa.gov/data/CALIPSO/>. Software—Figure 1 were drawn with Microsoft Paint (more information by checking <https://support.microsoft.com/en-us/windows/get-microsoft-paint-a6b9578c-ed1c-5b09-0699-4ed8115f9aa9>), Figure 2 were made with Python Matplotlib version 3.5.1 (Hunter, 2007), and other figures were made with IDL version 8.3, available at <https://www.harrisgeospatial.com/Software-Technology/IDL>.

## Acknowledgments

This research has been funded by the NASA Cloud, Aerosol and Monsoon Processes-Philippines Experiment (CAMP<sup>2</sup>Ex) field campaign under the research Grant 80NSSC18K0144 and 80NSSC21K1449. We acknowledge the Cloud-Aerosol Lidar and Infrared Pathfinder Satellite Observations science team for generating the aerosol products. We thank the NASA Langley Research Center's efforts in proving the data products and service.

## References

- Alfaro-Contreras, R., Zhang, J., Campbell, J. R., & Reid, J. S. (2016). Investigating the frequency and interannual variability in global above-cloud aerosol characteristics with CALIOP and OMI. *Atmospheric Chemistry and Physics*, 16(1), 47–69. <https://doi.org/10.5194/acp-16-47-2016>
- Andreae, M. O., & Rosenfeld, D. (2008). Aerosol-cloud-precipitation interactions. Part 1. The nature and sources of cloud-active aerosols. *Earth-Science Reviews*, 89(1–2), 13–41. <https://doi.org/10.1016/j.earscirev.2008.03.001>
- Balmes, K. A., & Fu, Q. (2021). All-sky aerosol direct radiative effects at the ARM SGP site. *Journal of Geophysical Research: Atmospheres*, 126(17). <https://doi.org/10.1029/2021JD034933>
- Burton, S. P., Ferrare, R. A., Hostetler, C. A., Hair, J. W., Rogers, R. R., & Obland, M. D. (2012). Aerosol classification using airborne High Spectral Resolution Lidar measurements-methodology and examples. *Atmospheric Measurement Techniques*, 5(1), 73–98. <https://doi.org/10.5194/amt-5-73-2012>

- Chand, D., Wood, R., Anderson, T. L., Satheesh, S. K., & Charlson, R. J. (2009). Satellite-derived direct radiative effect of aerosols dependent on cloud cover. *Nature Geoscience*, 2(3), 181–184. <https://doi.org/10.1038/ngeo437>
- Chang, I., & Christopher, S. A. (2017). The impact of seasonalities on direct radiative effects and radiative heating rates of absorbing aerosols above clouds. *Quarterly Journal of the Royal Meteorological Society*, 143(704), 1395–1405. <https://doi.org/10.1002/qj.3012>
- Christensen, M. W., & Stephens, G. L. (2011). Microphysical and macrophysical responses of marine stratocumulus polluted by underlying ships: Evidence of cloud deepening. *Journal of Geophysical Research*, 116(3), 1–10. <https://doi.org/10.1029/2010JD014638>
- Chung, C. E., Lewinschal, A., & Wilcox, E. (2016). Relationship between low-cloud presence and the amount of overlying aerosols. *Atmospheric Chemistry and Physics*, 16(9), 5781–5792. <https://doi.org/10.5194/acp-16-5781-2016>
- Devasthale, A., & Thomas, M. A. (2011). A global survey of aerosol-liquid water cloud overlap based on four years of CALIPSO-CALIOP data. *Atmospheric Chemistry and Physics*, 11(3), 1143–1154. <https://doi.org/10.5194/acp-11-1143-2011>
- Dey, S., & Di Girolamo, L. (2010). A climatology of aerosol optical and microphysical properties over the Indian subcontinent from 9 years (2000–2008) of Multiangle Imaging Spectroradiometer (MISR) data. *Journal of Geophysical Research*, 115(15), 1–22. <https://doi.org/10.1029/2009JD013395>
- Di Girolamo, L., Holz, R., Reid, J., Tanelli, S., & Heaver, S. V. D. (2018). *Cloud and aerosol monsoonal processes-Philippines experiment (CAMP2Ex)*, 1–30. Retrieved from [https://espo.nasa.gov/CAMP2Ex\\_White\\_Paper](https://espo.nasa.gov/CAMP2Ex_White_Paper)
- Grythe, H., Ström, J., Krejci, R., Quinn, P., & Stohl, A. (2014). A review of sea-spray aerosol source functions using a large global set of sea salt aerosol concentration measurements. *Atmospheric Chemistry and Physics*, 14(3), 1277–1297. <https://doi.org/10.5194/acp-14-1277-2014>
- Hong, Y., & Di Girolamo, L. (2020). Cloud phase characteristics over southeast Asia from A-Train satellite observations. *Atmospheric Chemistry and Physics*, 20, 8267–8291. <https://doi.org/10.5194/acp-20-8267-2020>
- Hong, Y., & Liu, G. (2015). The characteristics of ice cloud properties derived from CloudSat and CALIPSO measurements. *Journal of Climate*, 28, 3880–3901. <https://doi.org/10.1175/JCLI-D-14-00666.1>
- Hong, Y., Liu, G., & Li, J.-L. F. (2016). Assessing the radiative effects of global ice clouds based on CloudSat and CALIPSO measurements. *Journal of Climate*, 29, 7651–7674. <https://doi.org/10.1175/JCLI-D-15-0799.1>
- Hunter, J. D. (2007). Matplotlib: A 2D graphics environment. *Computing in Science & Engineering*, 9(3), 90–95. <https://doi.org/10.1109/MCSE.2007.55>
- IPCC. (2021). *Climate change 2021: The physical science basis. Contribution of working group I to the sixth assessment report of the intergovernmental panel on climate change*. Cambridge University Press.
- Kacenelenbogen, M., Redemann, J., Vaughan, M. A., Omar, A. H., Russell, P. B., Burton, S., et al. (2014). An evaluation of CALIOP/CALIPSO's aerosol-above-cloud detection and retrieval capability over North America. *Journal of Geophysical Research: Atmospheres*, 119(1), 230–244. <https://doi.org/10.1002/2013JD020178>
- Keil, A., & Haywood, J. M. (2003). Solar radiative forcing by biomass burning aerosol particles during SAFARI 2000: A case study based on measured aerosol and cloud properties. *Journal of Geophysical Research*, 108(13), 1–10. <https://doi.org/10.1029/2002jd002315>
- Kim, M.-H., Omar, A. H., Tackett, J. L., Vaughan, M. A., Winker, D. M., Trepte, C. R., et al. (2018). The CALIPSO version 4 automated aerosol classification and lidar ratio selection algorithm. *Atmospheric Measurement Techniques*, 11, 6107–6135. <https://doi.org/10.5194/amt-11-6107-2018>
- Kim, S. W., Yoon, S. C., Kim, J., & Kim, S. Y. (2007). Seasonal and monthly variations of columnar aerosol optical properties over East Asia determined from multi-year MODIS, LIDAR, and AERONET Sun/sky radiometer measurements. *Atmospheric Environment*, 41(8), 1634–1651. <https://doi.org/10.1016/j.atmosenv.2006.10.044>
- King, M. D., Platnick, S., Menzel, W. P., Ackerman, S. A., & Hubanks, P. A. (2013). Spatial and temporal distribution of clouds observed by MODIS onboard the Terra and Aqua satellites. *IEEE Transactions on Geoscience and Remote Sensing*, 51, 3826–3852. <https://doi.org/10.1109/TGRS.2012.2227333>
- Klein, S. A., & Hartmann, D. L. (1993). The seasonal cycle of low stratiform clouds. *Journal of Climate*, [https://doi.org/10.1175/1520-0442\(1993\)006<1587:tscols>2.0.co;2](https://doi.org/10.1175/1520-0442(1993)006<1587:tscols>2.0.co;2)
- Lebsack, M. D., Stephens, G. L., & Kummerow, C. (2008). Multisensor satellite observations of aerosol effects on warm clouds. *Journal of Geophysical Research*, 113(15), 1–12. <https://doi.org/10.1029/2008JD009876>
- Liao, H., & Seinfeld, J. H. (1998). Effect of clouds on direct aerosol radiative forcing of climate. *Journal of Geophysical Research*, 103(D4), 3781–3788. <https://doi.org/10.1029/97JD03455>
- Liu, Z., Kar, J., Zeng, S., Tackett, J., Vaughan, M., Avery, M., et al. (2019). *Discriminating between clouds and aerosols in the CALIOP version 4.1 data products, 2006* (pp. 703–734). <https://doi.org/10.5194/amt-12-703-2019>
- Liu, Z., Vaughan, M., Winker, D., Kittaka, C., Getzewich, B., Kuehn, R., et al. (2009). The CALIPSO lidar cloud and aerosol discrimination: Version 2 algorithm and initial assessment of performance. *Journal of Atmospheric and Oceanic Technology*, 26(7), 1198–1213. <https://doi.org/10.1175/2009JTECHA1229.1>
- Loeb, N. G., & Manalo-Smith, N. (2005). Top-of-atmosphere direct radiative effect of aerosols over global oceans from merged CERES and MODIS observations. *Journal of Climate*, 18(17), 3506–3526. <https://doi.org/10.1175/JCLI3504.1>
- Lohmann, U., & Feichter, J. (2005). Global indirect aerosol effects: A review. *Atmospheric Chemistry and Physics*, 5, 715–737. <https://doi.org/10.5194/acp-5-715-2005>
- Mallet, M., Solomon, F., Roblou, L., Peers, F., Turquety, S., Waquet, F., et al. (2017). Simulation of optical properties and direct and indirect radiative effects of smoke aerosols over marine stratocumulus clouds during Summer 2008 in California with the regional climate model RegCM. *Journal of Geophysical Research: Atmospheres*, 122(19), 10312–10337. <https://doi.org/10.1002/2017JD026905>
- Mao, K. B., Ma, Y., Xia, L., Chen, W. Y., Shen, X. Y., He, T. J., & Xu, T. R. (2014). Global aerosol change in the last decade: An analysis based on MODIS data. *Atmospheric Environment*, 94, 680–686. <https://doi.org/10.1016/j.atmosenv.2014.04.053>
- Matus, A. V., & L'Ecuyer, T. S. (2017). The role of cloud phase in Earth's radiation budget. *Journal of Geophysical Research: Atmospheres*, 2559–2578. <https://doi.org/10.1002/2016JD025951>
- Matus, A. V., L'Ecuyer, T. S., Kay, J. E., Hannay, C., & Lamarque, J.-F. (2015). The role of clouds in modulating global aerosol direct radiative effects in spaceborne active observations and the community Earth system model. *Journal of Climate*, 28(8), 2986–3003. <https://doi.org/10.1175/JCLI-D-14-00426.1>
- Mehta, M., Singh, R., Singh, A., Singh, N., & Anshumali (2016). Recent global aerosol optical depth variations and trends—A comparative study using MODIS and MISR level 3 datasets. *Remote Sensing of Environment*, 181, 137–150. <https://doi.org/10.1016/j.rse.2016.04.004>
- Meyer, K., Platnick, S., Oreopoulos, L., & Lee, D. (2013). Estimating the direct radiative effect of absorbing aerosols overlying marine boundary layer clouds in the southeast Atlantic using MODIS and CALIOP. *Journal of Geophysical Research: Atmospheres*, 118(10), 4801–4815. <https://doi.org/10.1002/jgrd.50449>

- Mishchenko, M. I., Geogdzhayev, I. V., Cairns, B., Carlson, B. E., Chowdhary, J., Lacis, A. A., et al. (2007). Past, present, and future of global aerosol climatologies derived from satellite observations: A perspective. *Journal of Quantitative Spectroscopy and Radiative Transfer*, 106(1–3), 325–347. <https://doi.org/10.1016/j.jqsrt.2007.01.007>
- NASA/LARC/SD/ASDC. (2018a). CALIPSO lidar level 25 km merged layer, V4-20. NASA Langley Atmospheric Science Data Center DAAC. [https://doi.org/10.5067/CALIOP/CALIPSO/LID\\_L2\\_05KMMLAY-STANDARD-V4-20](https://doi.org/10.5067/CALIOP/CALIPSO/LID_L2_05KMMLAY-STANDARD-V4-20)
- NASA/LARC/SD/ASDC. (2018b). CALIPSO lidar level 2 aerosol profile, V4-20. NASA Langley Atmospheric Science Data Center DAAC. [https://doi.org/10.5067/CALIOP/CALIPSO/LID\\_L2\\_05KMAPRO-STANDARD-V4-20](https://doi.org/10.5067/CALIOP/CALIPSO/LID_L2_05KMAPRO-STANDARD-V4-20)
- Omar, A. H., Winker, D. M., Kittaka, C., Vaughan, M. A., Liu, Z., Hu, Y., et al. (2009). The CALIPSO automated aerosol classification and lidar ratio selection algorithm. *Journal of Atmospheric and Oceanic Technology*, 26(10), 1994–2014. <https://doi.org/10.1175/2009JTECHA1231.1>
- Palacios-Peña, L., Jiménez-Guerrero, P., Baró, R., Balzarini, A., Bianconi, R., Curci, G., et al. (2019). Aerosol optical properties over Europe: An evaluation of the AQMEII Phase 3 simulations against satellite observations. *Atmospheric Chemistry and Physics*, 19(5), 2965–2990. <https://doi.org/10.5194/acp-19-2965-2019>
- Rauber, R. M., Zhao, G., Girolamo, L. D., & Colón-Robles, M. (2013). Aerosol size distribution, particle concentration, and optical property variability near Caribbean trade cumulus clouds: Isolating effects of vertical transport and cloud processing from humidification using aircraft measurements. *Journal of the Atmospheric Sciences*, 70(10), 3063–3308. <https://doi.org/10.1175/JAS-D-12-0105.1>
- Remer, L. A., Kleidman, R. G., Levy, R. C., Kaufman, Y. J., Tanré, D., Mattoe, S., et al. (2008). Global aerosol climatology from the MODIS satellite sensors. *Journal of Geophysical Research*, 113(14), 1–18. <https://doi.org/10.1029/2007JD009661>
- Rogers, R. R., Vaughan, M. A., Hostetler, C. A., Burton, S. P., Ferrare, R. A., Young, S. A., et al. (2014). Looking through the haze: Evaluating the CALIPSO level 2 aerosol optical depth using airborne high spectral resolution lidar data. *Atmospheric Measurement Techniques*, 7(12), 4317–4340. <https://doi.org/10.5194/amt-7-4317-2014>
- Rosenfeld, D., Andreae, M. O., Asmi, A., Chin, M., Leeuw, G., Donovan, D. P., et al. (2014). Global observations of aerosol-cloud-precipitation-climate interactions. *Reviews of Geophysics*, 52, 750–808. <https://doi.org/10.1002/2013RG000441>
- Rosenfeld, D., Zhu, Y., Wang, M., Zheng, Y., Goren, T., & Yu, S. (2019). Aerosol-driven droplet concentrations dominate coverage and water of oceanic low-level clouds. *Science*, 363(6427), eaav0566. <https://doi.org/10.1126/science.aav0566>
- Ross, A. D., Holz, R. E., Quinn, G., Reid, J. S., Xian, P., Joseph Turk, F., & Posselt, D. J. (2018). Exploring the first aerosol indirect effect over southeast Asia using a 10-year collocated MODIS, CALIOP, and model dataset. *Atmospheric Chemistry and Physics*, 18, 12747–12764. <https://doi.org/10.5194/acp-18-12747-2018>
- Sassen, K., & Wang, Z. (2008). Classifying clouds around the globe with the CloudSat radar: 1-year of results. *Geophysical Research Letters*, 35, L04805. <https://doi.org/10.1029/2007GL032591>
- Sassen, K., Wang, Z., & Liu, D. (2008). Global distribution of cirrus clouds from CloudSat/cloud-aerosol lidar and infrared pathfinder satellite observations (CALIPSO) measurements. *Journal of Geophysical Research*, 113, D00A12. <https://doi.org/10.1029/2008JD009972>
- Schulze, B. C., Charan, S. M., Kenseth, C. M., Kong, W., Bates, K. H., Williams, W., et al. (2020). Characterization of aerosol hygroscopicity over the northeast Pacific Ocean: Impacts on prediction of CCN and stratocumulus cloud droplet number concentrations. *Earth and Space Science*, 7(7). <https://doi.org/10.1029/2020EA001098>
- Shinozuka, Y., Kacenelenbogen, M., Burton, S., Howell, S., Zuidema, P., Ferrare, R., et al. (2020). Daytime aerosol optical depth above low-level clouds is similar to that in adjacent clear skies at the same heights: Airborne observation above the southeast Atlantic. *Atmospheric Chemistry and Physics*, 1–26. <https://doi.org/10.5194/acp-2019-1007>
- Sivaprasad, P., & Babu, C. A. (2014). Seasonal variation and classification of aerosols over an inland station in India. *Meteorological Applications*, 21(2), 241–248. <https://doi.org/10.1002/met.1319>
- Su, W., Schuster, G. L., Loeb, N. G., Rogers, R. R., Ferrare, R. A., Hostetler, C. A., et al. (2008). Aerosol and cloud interaction observed from high spectral resolution lidar data. *Journal of Geophysical Research*, 113(24), 1–9. <https://doi.org/10.1029/2008JD010588>
- Tackett, J. L., & Di Girolamo, L. (2009). Enhanced aerosol backscatter adjacent to tropical trade wind clouds revealed by satellite-based lidar. *Geophysical Research Letters*, 36(14), 1–5. <https://doi.org/10.1029/2009GL039264>
- Tackett, J. L., Winker, D. M., Getzewich, B. J., Vaughan, M. A., Young, S. A., & Kar, J. (2018). CALIPSO lidar level 3 aerosol profile product: Version 3 algorithm design. *Atmospheric Measurement Techniques*, 11(7), 4129–4152. <https://doi.org/10.5194/amt-11-4129-2018>
- Tan, S., Han, Z., Wang, B., & Shi, G. (2017). Variability in the correlation between satellite-derived liquid cloud droplet effective radius and aerosol index over the northern Pacific Ocean. *Tellus B: Chemical and Physical Meteorology*, 69(1), 1391656. <https://doi.org/10.1080/16000889.2017.1391656>
- Ten Hoeve, J. E., & Augustine, J. A. (2016). Aerosol effects on cloud cover as evidenced by ground-based and space-based observations at five rural sites in the United States. *Geophysical Research Letters*, 43(2), 793–801. <https://doi.org/10.1002/2015GL066873>
- Thorsen, T. J., Ferrare, R. A., Hostetler, C. A., Vaughan, M. A., & Fu, Q. (2017). The impact of lidar detection sensitivity on assessing aerosol direct radiative effects. *Geophysical Research Letters*, 44(17), 9059–9067. <https://doi.org/10.1002/2017GL074521>
- Thorsen, T. J., & Fu, Q. (2015). CALIPSO-inferred aerosol direct radiative effects: Bias estimates using ground-based Raman lidars. *Journal of Geophysical Research*, 120(23), 12209–12220. <https://doi.org/10.1002/2015JD024095>
- Várnai, T., & Marshak, A. (2015). Effect of cloud fraction on near-cloud aerosol behavior in the MODIS atmospheric correction ocean color product. *Remote Sensing*, 7(5), 5283–5299. <https://doi.org/10.3390/rs70505283>
- Vaughan, M. A., Powell, K. A., Kuehn, R. E., Young, S. A., Winker, D. M., Hostetler, C. A., et al. (2009). Fully automated detection of cloud and aerosol layers in the CALIPSO lidar measurements. *Journal of Atmospheric and Oceanic Technology*, 26(10), 2034–2050. <https://doi.org/10.1175/2009JTECHA1228.1>
- Winker, D. M., Pelon, J. R., & McCormick, M. P. (2003). The CALIPSO mission: Spaceborne lidar for observation of aerosols and clouds. *Lidar Remote Sensing for Industry and Environment Monitoring III*, 1–11, 4893. <https://doi.org/10.1117/12.466539>
- Winker, D. M., Tackett, J. L., Getzewich, B. J., Liu, Z., Vaughan, M. A., & Rogers, R. R. (2013). The global 3-D distribution of tropospheric aerosols as characterized by CALIOP. *Atmospheric Chemistry and Physics*, 13(6), 3345–3361. <https://doi.org/10.5194/acp-13-3345-2013>
- Winker, D. M., Vaughan, M. A., Omar, A., Hu, Y., Powell, K. A., Liu, Z., et al. (2009). Overview of the CALIPSO mission and CALIOP data processing algorithms. *Journal of Atmospheric and Oceanic Technology*, 26(11), 2310–2323. <https://doi.org/10.1175/2009JTECHA1281.1>
- Wu, X., Balmes, K. A., & Fu, Q. (2021). Aerosol direct radiative effects at the ARM SGP and TWP sites: Clear skies. *Journal of Geophysical Research: Atmospheres*, 126(5), 1–24. <https://doi.org/10.1029/2020JD033663>
- Xian, P., Klotzbach, P., Dunion, J., Janiga, M., Reid, J., Colarco, P., & Kipling, Z. (2020). Revisiting the relationship between Atlantic dust and tropical cyclone activity using aerosol optical depth reanalyses: 2003–2018. *Atmospheric Chemistry and Physics*, 1–43. <https://doi.org/10.5194/acp-2020-287>
- Xu, H., Guo, J., Wang, Y., Zhao, C., Zhang, Z., Min, M., et al. (2017). Warming effect of dust aerosols modulated by overlapping clouds below. *Atmospheric Environment*, 166, 393–402. <https://doi.org/10.1016/j.atmosenv.2017.07.036>

- Yang, W., Marshak, A., Várnai, T., Kalashnikova, O. V., & Kostinski, A. B. (2012). CALIPSO observations of transatlantic dust: Vertical stratification and effect of clouds. *Atmospheric Chemistry and Physics*, 12(23), 11339–11354. <https://doi.org/10.5194/acp-12-11339-2012>
- Young, S. A., & Vaughan, M. A. (2009). The retrieval of profiles of particulate extinction from cloud-aerosol lidar infrared pathfinder satellite observations (CALIPSO) data: Algorithm description. *Journal of Atmospheric and Oceanic Technology*, 26(6), 1105–1119. <https://doi.org/10.1175/2008JTECH1221.1>
- Young, S. A., Vaughan, M. A., Kuehn, R. E., & Winker, D. M. (2013). The retrieval of profiles of particulate extinction from Cloud-Aerosol Lidar and Infrared Pathfinder Satellite Observations (CALIPSO) data: Uncertainty and error sensitivity analyses. *Journal of Atmospheric and Oceanic Technology*, 30(3), 395–428. <https://doi.org/10.1175/JTECH-D-12-00046.1>
- Young, S. A., Winker, D. M., Hu, Y., & Kuehn, R. E. (2008). *CALIOP algorithm theoretical basis document, Part 4: Extinction retrieval algorithms theoretical basis documents*. Retrieved from <http://scholar.google.com/scholar?hl=en&btnG=Search&q=intitle:CALIOP+Algorithm+Theoretical+Basis+Document+Part+3+:+Scene+Classification+Algorithms#>
- Zhang, Z., Meyer, K., Yu, H., Platnick, S., Colarco, P., Liu, Z., & Oreopoulos, L. (2016). Shortwave direct radiative effects of above-cloud aerosols over global oceans derived from 8 years of CALIOP and MODIS observations. *Atmospheric Chemistry and Physics*, 16(5), 2877–2900. <https://doi.org/10.5194/acp-16-2877-2016>